The Emerald Research Register for this journal is available at
**www.emeraldinsight.com/researchregister**

The current issue and full text archive of this journal is available at
**www.emeraldinsight.com/0961-5539.htm**



# A model of heat transfer dynamics of coupled multiphase-flow and neutron-radiation

## Application to a nuclear fluidized bed reactor

Received May 2003
Revised October 2004
Accepted February 2005

C.C. Pain, J.L.M.A. Gomes, M.D. Eaton, C.R.E. de Oliveira and A.J.H. Goddard

*Department of Earth Sciences and Engineering, Imperial College London, London, UK*

### Abstract

**Purpose** – To present dynamical analysis of axisymmetric and three-dimensional (3D) simulations of a nuclear fluidized bed reactor. Also to determine the root cause of reactor power fluctuations.

**Design/methodology/approach** – We have used a coupled neutron radiation (in full phase space) and high resolution multiphase gas-solid Eulerian-Eulerian model.

**Findings** – The reactor can take over 5 min after start up to establish a quasi-steady-state and the mechanism for the long term oscillations of power have been established as a heat loss/generation mechanism. There is a clear need to parameterize the temperature of the reactor and, therefore, its power output for a given fissile mass or reactivity. The fission-power fluctuates by an order of magnitude with a frequency of 0.5-2 Hz. However, the thermal power output from gases is fairly steady.

**Research limitation/implications** – The applications demonstrate that a simple surrogate of a complex model of a nuclear fluidised bed can have a predictive ability and has similar statistics to the more complex model.

**Practical implications** – This work can be used to analyze chaotic systems and also how the power is sensitive to fluctuations in key regions of the reactor.

**Originality/value** – The work presents the first 3D model of a nuclear fluidised bed reactor and demonstrates the value of numerical methods for modelling new and existing nuclear reactors.

**Keywords** Flow, Heat transfer, Nuclear reactors, Numerical analysis

**Paper type** Research paper

### Nomenclature

| | | | |
|---|---|---|---|
| $v$ | = velocity, $\mathrm{m\,s^{-1}}$ | $g$ | = gravitational constant, $\mathrm{m\,s^{-2}}$ |
| $t$ | = time, s | $p$ | = pressure, Pa ($\mathrm{N\,m^{-2}}$) |
| $\mathbf{r}$ | = position vector | $C$ | = specific heat capacity, $\mathrm{J\,kg^{-1}\,K^{-1}}$ |
| $x$, $y$ | = coordinates | | |

The authors would like to thank Professor R.T. Ackroyd and Professor M.M.R. Williams for their invaluable help and advice. The authors would like to thank the HSE for funding the development of the FETCH model used in this study. Dr Gomes is supported by CAPES/Brazil and by UERJ(PROCASE)/Brazil.



0961-5539
DOI 10.1108/09615530510625084

$T$ = temperature, K
$q$ = flux of fluctuation energy, $kg\,m^{-1}s^{-3}$
$C_d(\mathbf{r}, t)$ = $d$-th delayed group precursor concentration
$E$ = neutron energy (eV)
$S_f(\mathbf{r}, t)$ = fission heat source, $cm^{-3}s^{-1}$
$S(\mathbf{r}, \Omega, E, t)$ = neutron source, $cm^{-3}s^{-1}\,ev^{-1}sr^{-1}$
$\Sigma_f(\mathbf{r}, t)$ = macroscopic fission cross section, $cm^{-1}$

*Subscripts*
k = phase(f = fluid, s = solid)
$i,j$ = $x,y$-directions
w = wall

*Greek symbols*
$\mathscr{H}$ = scattering-removal operator
$\lambda_d$ = decay constant ($\beta$ decay) of $d$-th precursor group, $s^{-1}$
$\beta_d$ = fraction of all fission neutrons (both prompt and delayed) emitted per fission that appear from the $d$-th precursor group
$\phi(\mathbf{r}, E, t)$ = neutron scalar flux, $cm^{-2}s^{-1}eV^{-1}$
$\phi(\mathbf{r}, \Omega, E, t)$ = neutron angular flux, $cm - 2s^{-1}eV^{-1}sr^{-1}$
$\varepsilon$ = volume fraction
$\rho$ = density, $kg\,m^{-3}$
$\Gamma$ = frictional force exerted on the wall by the phase, $N\,m^{-4}s$
$\alpha$ = volumetric interphase heat transfer coefficient, $W\,m^{-3}K^{-1}$
$\Omega$ = volumetric wall-phase heat transfer coefficient, $W\,m^{-3}K^{-1}$
$\Theta$ = granular temperature, $m^2s^{-2}$
$\gamma$ = collisional energy dissipation, $kg\,m^{-1}s^{-3}$
$\kappa$ = thermal conductivity, $W\,m^{-1}K^{-1}$
$\Omega$ = direction of neutron travel

## Introduction

Nuclear reactor concepts based on gas fluidization of fine uranium fuel pellets have attracted considerable attention over the years (Yamamoto, 1995; van Dam *et al.*, 1997; Golovko *et al.*, 1999). Reasons behind this interest lies in their excellent heat transfer capabilities and the mixing abilities of fluidized beds (Kunii and Levenspiel, 1991). The latter unifies the temperature of the bed, and increases the active surface area from which heat transfer occurs. In addition, the constant mixing of the bed potentially leads to a uniform burn-up of the uranium particles. A self-controlling feature is also present in that as the bed is fluidized and the gas flow increases, the power achieves a maximum at a particular bed height. At this height, the power will be that at which fission-heat production is balanced by heat losses in a time averaged sense.

A possible disadvantage of such a reactor is the chaotic particle flow characteristics of the fluidized bed in which large bubbles and slugs propagate through it (Smolders and Baeyens, 2001; Stewart and Davidson, 1967), changing the geometry and nuclear criticality. This will impact on the fission rate which will also be highly variable – although it is possible that the power output obtained from the heated gases may not be as variable. This variability and chaotic unpredictability requires further investigation in order that the concept can be assessed.

Deterministic chaos theory offers a powerful description of irregular behavior and anomalies in systems which do not seem to be stochastic. In such systems, small perturbations in the initial conditions lead to large discrepancies in the final solution (Anishchenko, 1995). Indeed, chaos theory applied to the output signals is a useful tool for the understanding of nonlinear systems as demonstrated by its application to the nuclear reactor investigated in this work. It is often used to quantify the regime (e.g. bubbling and slugging) that fluidized beds operate in Huilin *et al.* (1995) and Johnsson *et al.* (2000).

Power variability in a nuclear fluidized bed reactor has been studied by van Dam *et al.* (1997) who investigated the sensitivity of the reactor to voidage fluctuations. This reactor concept adopts aspects of the pebble bed reactor (Gerwin and Scherer, 1987) and the fuel particles are of a design as reported by Gulden and Nickel (1977) (Golovko *et al.*, 1999). Other reactor designs of this type are described by Sefidvash (1996).

The modelling approach developed by the authors applies detailed spatial/temporal modelling so that the reactor dynamics evolve naturally. This is in contrast to point kinetics models (Hetrick, 1993) which, although often having adequate accuracy, require correlation with existing data when the material evolves within the transient, such as in fissile liquid transients (Mather *et al.*, 1994; Mather and Barbry, 1991) and nuclear fluidized beds. Others have used space-dependent kinetics to model transients in fissile liquids, see Kimpland and Korneich (1996), Yamamoto (1995) and Rifat *et al.* (1993). Some point kinetics models for powders are reported by Rozain (1991) and Basoglu *et al.* (1994), and for the nuclear fluidized bed models (Golovko *et al.*, 2000a, b, c).

An integrated neutrons/fluids/heat transfer method embodied in the finite element transient criticality (FETCH) model (Pain *et al.*, 1998a, 2001a), is used here. The neutronics model in FETCH solves the neutron Boltzmann transport equation in full phase-space (space, time, angle and speed travel) using a variational finite element approach based on the second order even parity equations (de Oliveira *et al.*, 1998). The fluids algorithm is a high-resolution multiphase compressible flow model which solves the conservation equations for both gas and solid particle phases (Pain *et al.*, 2001e). This unique fundamentally based combined methodology is able to model the complex non-linear reactivity feedback mechanisms which may occur in nuclear reactor designs such as the one studied in this paper. The FETCH model used here has been compared against solution transient criticality experiments (Pain *et al.*, 2001b, c, 1998a) and fluidized bed experiments (Pain *et al.*, 2001d, 2002a).

The two-fluid granular temperature method (TFGTM) was chosen to model the gas-solid flow in the nuclear fluidized bed. Within the solid phase, particle modelling is based on an analogy between the kinetic theory of gases and binary particle-particle collisions (Lun *et al.*, 1984; Johnson and Jackson, 1987; Jenkins and Savage, 1983). These models are proving to be accurate for a wide range of gas-solid fluidization scenarios (Samuelsberg and Hjertager, 1996; Ding and Gidaspow, 1990).

A secondary aim (other than investigating the dynamics of this reactor) of this paper is to investigate the numerical convergence in space and direction of angle of neutron travel of a conceptual 2D and 3D nuclear fluidized bed reactor. This will help demonstrate the robustness of the numerical techniques introduced by Pain *et al.* (2003b) (Pain *et al.*, 2002b). These new numerical techniques are globally high order accurate in space and time and may be used to resolve detailed spatially evolving fields in a coupled high-resolution multiphase-flow and neutron-radiation dynamics in nuclear fluidized bed reactors. In addition, a numerical investigation of the route cause and sensitivity of particle concentration to fission-power variability is conducted. In the latter we also developed a surrogate model of fission-power and reactor temperature.

In the next section, the Boltzmann neutron transport equations and the two-fluid granular temperature equations are presented. The model used to solve this coupled systems is summarized. The dynamics of 2D nuclear fluidized bed reactors are explained and the grid dependence investigated. Numerical simulations conducted in 3D geometry are then shown. Dynamic analysis is then applied to fission-power and voidage time series to investigate the bubbles dynamics and the relationship between bubble production and fission power. A surrogate method is then proposed to predict both fission-power and reactor temperature over a short time interval. Conclusions are drawn in the final section.

## The nuclear fluidized bed reactor model

With the rapid development of robust numerical techniques and corresponding computer codes there has been an increasing trend toward modelling more and more complex phenomena and in particular to model strongly coupled multi-physics phenomena, e.g. fluid/structure interactions and fluids/radiation. The latter, the focus of the applications in this paper, include radiation fluids applications from the atmosphere (fluids and cloud radiation), exchanges in stars, thermal radiation resulting from combustion problems (Kunii and Levenspiel, 1991), and coupled neutron radiation and fluids problems for reactivity assessment in fissile solutions (Pain *et al.*, 1998a, b, 2001b), nuclear reactors (Sefidvash, 1996) including the novel thermal nuclear reactor studied here (Pain *et al.*, 2002b, 2003a; Golovko *et al.*, 2000c).

The numerical methods used in this work (Pain *et al.*, 2003b) are robust in a wide range of situations. They are applied to model a helium cooled nuclear fluidized bed reactor. Indeed, fluidized beds are characterized by sharp solids gradients and rapid transient behavior. Therefore, they are stern tests for the numerical methods developed to solve the set of non-linear differential conservative equations. In addition, due to the mixing properties, heat and mass transfer processes are efficient in fluidized beds, which make them excellent devices for power generation. However, due to the chaotic fluidization characteristics, power generation from nuclear fuels may be difficult to control and, therefore, may need feedback controls. Hence, a technique was developed to predict, in a statistical sense, the fission rate over a short time interval.

### *Neutronics*

The Boltzmann neutron transport equation (Table I) is solved using finite elements in space, spherical harmonics ($P_N$) in angle, multigroup in energy and implicit two level time discretization methods. Such methods were applied using the second-order even-parity variational principle as described by de Oliveira *et al.* (1998). This equation is solved in full seven dimension phase space. Six energy groups where used and where obtained by collapsing the original WIMS 69 group library taking into account resonant self shielding and particle spatial effects into six energy groups (see WIMS, 1999). A set of cross-sections are generated for various temperatures and these are used to obtain (with a temperature interpolation procedure) the local cross-section set for each element of the finite element mesh. Six delayed neutron precursor concentration groups (Duderstadt and Hamilton, 1976) are used in these simulations.

### *Two-fluid granular temperature model*

In the TFGTM, both phases are continuous and fully inter-penetrating, and are described by separated conservative equations with interaction terms representing the

| | |
|---|---|
| Continuity equation | $\frac{\partial}{\partial t}(\varepsilon_k \rho_k) + \frac{\partial}{\partial x_i}(\varepsilon_k \rho_k v_{ki}) = 0$ |
| Momentum equation | $\frac{\partial}{\partial t}(\varepsilon_k \rho_k v_{ki}) + \frac{\partial}{\partial x_j}(\varepsilon_k \rho_k v_{ki} v_{kj}) = -\varepsilon_k \frac{\partial p_g}{\partial x_i} + \varepsilon_k \rho_k g_i + \beta(v_{k'i} - v_{ki}) - \frac{\partial}{\partial xi}(\tau_{kij}) - \Gamma_k v_{ki}$ |
| Thermal energy equations | $C_{p_g} \rho_g \varepsilon_g \frac{DT_g}{Dt} = -p_g \left( \frac{\partial}{\partial x_i} \varepsilon_g v_{g_i} + \frac{\partial}{\partial x_i} \varepsilon_{\mathrm{s}} v_{s_i} \right) + \frac{\partial}{\partial x_i} \left( \varepsilon_g \kappa_g \frac{\partial T_g}{\partial x_i} \right) + \quad C_{p_{\mathrm{s}}} \rho_{\mathrm{s}} \varepsilon_{\mathrm{s}} \frac{DT_{\mathrm{s}}}{Dt} = \frac{\partial}{\partial x_i} \left( \varepsilon_{\mathrm{s}} \kappa_{\mathrm{s}} \frac{\partial T_{\mathrm{s}}}{\partial x_i} \right) + \alpha(T_g - T_{\mathrm{s}}) + S_{\mathrm{f}}$ |
| Granular energy equation | $\frac{3}{2}\left[ \frac{\partial(\varepsilon_{\mathrm{s}} \rho_{\mathrm{s}} \Theta)}{\partial t} + \frac{\partial}{\partial x_j}(\varepsilon_{\mathrm{s}} \rho_{\mathrm{s}} v_{s_j} \Theta) \right] = \tau_{s_{ij}} \frac{\partial v_{s_i}}{\partial x_j} - \frac{\partial q_j}{\partial x_j} - \gamma - 3\beta\Theta$ |
| Equation for $d$-th delayed neutron group precursor concentration | $\frac{\partial C_d(\mathbf{r},t)}{\partial t} + \frac{\partial v_{s_j} C_d(\mathbf{r},t)}{\partial x_j} = -\lambda_d C_d(\mathbf{r}, t) + \beta_d \int_0^\infty \nu \sum_{\mathrm{f}} \phi(\mathbf{r}, E, t)\, dE$ |
| Neutron transport equation | $\frac{1}{v}\frac{\partial \psi(\mathbf{r},\Omega,E,t)}{\partial t} + \Omega \Delta \psi(\mathbf{r}, \Omega, E, t) + \mathscr{H} \psi(\mathbf{r}, \Omega, E, t) = S(\mathbf{r}, \Omega, E, t)$ |

**Table I.** Conservation equations used in the simulations

coupling between the phases. The TFGTM requires additional closure laws to describe the rheology of the particulate phase. These closure laws are based on the assumptions of kinetic theory for granular flows (reviews can be found in Gidaspow, 1994). As the rheology of the granular phase was based on empirical correlations, Jenkins and Savage (1983) and Ding and Gidaspow (1990) proposed a model in which the solid viscosity and the normal stress are derived using an analogy between the particle-collision during granular flows and the gas kinetic theory. Hence, the concept of granular temperature as a measure of the agitation of particles was introduced. The granular temperature is, therefore, a link between kinetic theory and traditional fluid mechanics. The set of TFGTM conservative equations that describes the gas-solid flow and the additional closure laws are summarized in Pain *et al.* (2001e, 2002a).

The following sections provide an overview of the discretisation and solution methods used to solve the TFGTM equations, see Table I. The full description can be found in Pain *et al.* (2003b) (Pain *et al.*, 2001e).

*High resolution method.* A high resolution method is used in this work to achieve bounded physical meaningful solutions that are also highly accurate. The method used to limit the spatial derivatives is based on the NVD approach (Leonard, 1991) in which face variables are calculated from the element centered values of the field being solved. The variation of these face variables over each face is then limited using the NVD approach so that, if a local extrema is found, then the method switches to a first-order spatial discretisation. This switching is performed in a smooth manner and smoothly depends on a extrema-detecting variable.

A second order temporarily limited time stepping method (based on the Crank Nicholson method) is used in this work to help achieve bounded solutions, e. g. positive volume fraction.

*Momentum discretization.* To maintain consistency with the discretized continuity equation, pressure as well as volume fractions have a piecewise constant variation across each hexahedral element. For similar reasons the granular temperature equations are also discretised using the high-resolution method described above. The velocities have a tri-linear variation across each element and are thus centered on the nodes of the finite element mesh. The momentum equations are discretised using a Bubnov-Petrov-Galerkin method by multiplying each of the momentum equations for the three velocity components by finite element basis functions and integrating the resulting pressure term by parts. A non-linear Petrov-Galerkin method is used to suppress velocity oscillations normal to the flow direction. The momentum equations are discretised in time using implicit Crank-Nicholson time stepping, see Pain *et al.* (2001e) for further details.

A semi-implicit projection method is used to solve the coupled multiphase continuity and momentum equations. This method treats the coupling between the phases implicitly in pressure. A mixed finite element method with a constant variation of pressure throughout each element and a bi-linear variation of velocity is used here to avoid singularities in the discretised equations.

## 2D numerical simulations[1]

*Geometry*

The fluidized bed nuclear reactor comprises of an internal cavity 6 m tall and 1.25 m in diameter in which the fluidized fuel particles are free to move (Figure 1(a)). The particles are 1 mm in diameter TRISO coated spheres (Golovko *et al.*, 2000b) with an uranium kernel and have a moderator to fuel (uranium) content by volume of 300-1. The particles are described in Golovko *et al.* (1999). The internal cavity of the reactor is surrounded by graphite moderator which slows down the neutrons and reflects them back into the reactor. These slow neutrons are particularly effective at producing subsequent neutrons from fission reactions and thus the largest power density of the reactor tends to be situated near the walls of the reactor. It also means that as a large mass of particles approaches the wall of the reactor, the reactor responds with positive reactivity feedback. This provides the root source for the fission-power fluctuations in the reactor.

The graphite side, top and bottom walls of the reactor are 1 m in thickness. The graphite at the top and bottom of the reactor is porous. This porous graphite is a new design feature over previous design (Pain *et al.*, 2002b) which enables the reactor to be more sub-critical in the collapsed bed state and also provides a flatter reactivity ($K_{\text{eff}}$) curve versus uniformly expanded bed height. The reactivity of the system, measured by the eigen-value $K_{\text{eff}}$, is the ratio of the number of neutrons generated from one neutron generation to the next. Thus a flatter reactivity curve is safer, since if the system goes supercritical and deposits heat energy which expands the bed, there is not a positive reactivity feedback associated with this expansion. Curves showing the reactivity of the reactor system versus uniformly expanded bed height are shown in Figure 2(a) for different porosities. $K_{\text{eff}}$ in these figures is a measure of the criticality of the system of the neutron multiplication and from one neutron generation to the next. The initial bed porosity used in the simulations conducted here is 0.4.

The simulations were conducted in *r-z* geometry and the physical properties of both phases used in this work are outlined in Table II. In addition, the initial and boundary conditions are summarized in Table III and there is no heat loss to the walls. Several fields were obtained by solving the set of fluid and neutron transport equations, among

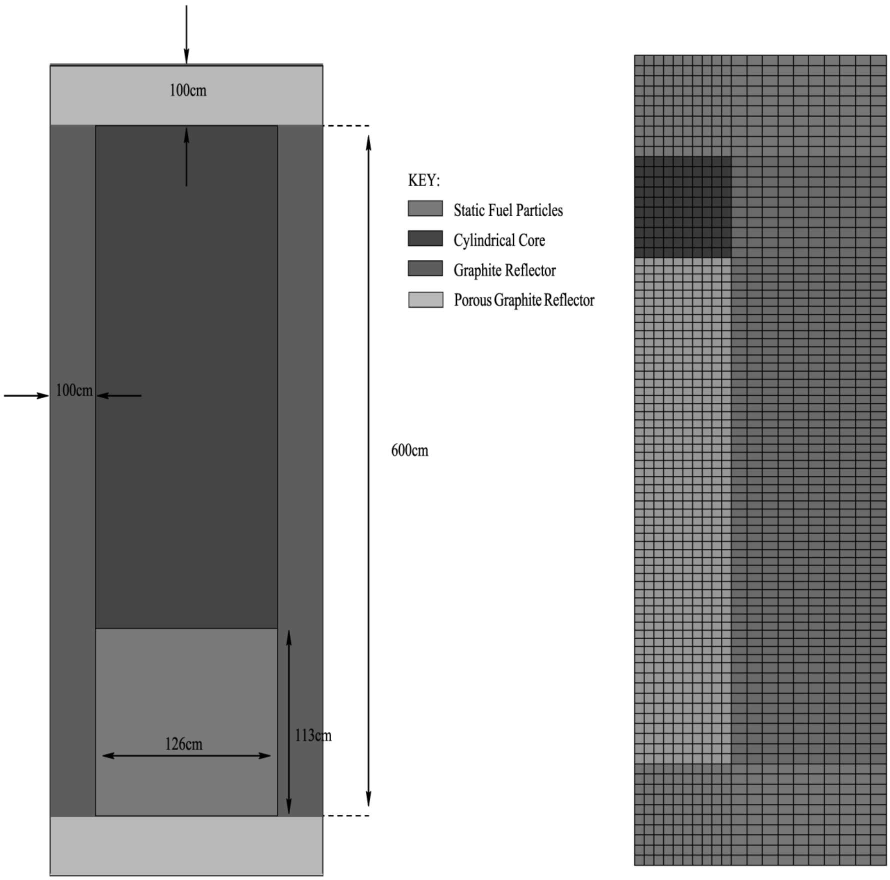


**(a)** 2-D schematic of the FLUBER reactor

**(b)** 2-D finite element mesh

**Note:** The coarse mesh is shown here, the corresponding fine mesh has twice the resolution in each direction

**Figure 1.** FLUBER reactor: (a) Schematic and (b) finite element mesh

them, the following will be directly used to demonstrate the robustness of the numerical methods advocated here: delayed neutrons concentration, solid volume fraction, temperature of both phases, granular temperature and the velocity components of the gas and solid phases. In order to investigate the time series of these fields, several detectors were placed within the bed as shown in Table IV.

In the simulations presented in the following sections (Figure 1(b)), the domain had (unless otherwise stated) 2,000 volume elements and 2,121 nodes, and the fluids occupied domain had 750 volume elements and 836 nodes.

*Physics of the reactor*

As the uranium particles are fluidized and the bed expands, the system becomes supercritical and so the fission heat source increases exponentially. The reactivity

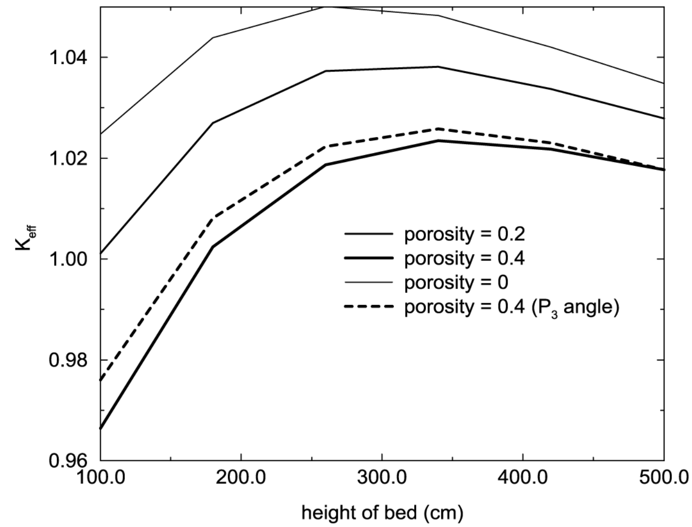


**(a)** K*eff* versus uniformly expanded height

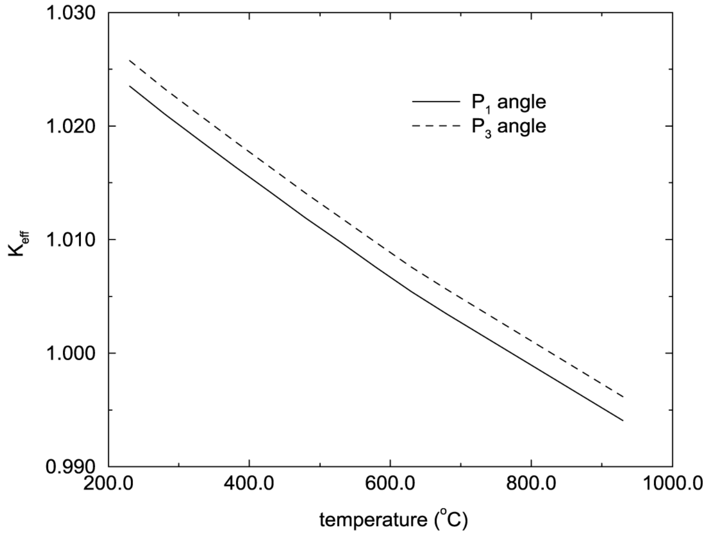


**(b)** K*eff* versus temperature

**Figure 2.**
The reactivity of the system ($K_{eff}$) versus uniformly expanded bed height

**Notes:** Graph shows reactivity for differing porosities of the graphite at the top and bottom of the reactor. In addition (b) shows the variation of $K_{eff}$ with temperature for a uniform bed height of 340 cm (measured by the eigenvalue and which determines the magnitude of the exponent) of the system increases on uniform bed expansion (bed height) as shown in Figure 2. This shows that during the bed expansion, the reactivity reaches a maximum and on further expansion of the bed the reactivity decreases due to the increasing in neutron leakage out of the system.

The reactivity of the system is enhanced due to the increasing in moderated and reflected neutrons back into the fluidized bed on its expansion. This reactor has been re-designed so that it is more subcritical in collapsed bed or fully expanded state. In particular the solid graphite walls surrounding the fluidized bed cavity have been replaced at the top and bottom of the reactor, see Figure 1(a), by porous graphite with a volume fraction of 60 percent. The effect on the reactivity, gauged by the eigen-value, is seen in Figure 2(a). The porous graphite provides for a flatter curve which is desirable on safety grounds. The response to void fluctuations near the bottom of the reactor is reduced with this modification – due to the neutrons not being reflected back, as readily, into the regions of high particle volume fraction near the bottom wall.

| | Solid phase | Gas phase |
|---|---|---|
| Density (kg m$^{-3}$) | $1.92 \times 10^3$ | Ideal gas law |
| Thermal Conductivity (W m$^{-1}$ K$^{-1}$) | 1.0 | $2.15 \times 10^{-1}$ |
| Heat capacity (J kg$^{-1}$ K$^{-1}$) | $1.40 \times 10^3$ | $5.24 \times 10^3$ |
| Particle diameter (m) | $1.00 \times 10^{-3}$ | – |
| Dynamic viscosity (kg m$^{-1}$ s$^{-1}$) | – | $2.70 \times 10^{-5}$ |

**Table II.** Physical properties of the solid (TRISO coated fuels spheres) and the gas (helium) phases

| | |
|---|---|
| Initial $\varepsilon_s$ | 0.40 |
| Inlet gas velocity | $v_f(r, z = 0, t) = 1.20\,\mathrm{m\,s^{-1}}$ |
| Inlet gas temperature | $T_f(r, z = 0, t) = 226.85°\mathrm{C}$ |
| Initial gas and solid phase velocities | $v_s(r, z, t = 0) = 0.0\,\mathrm{m\,s^{-1}}$<br>$v_f(r, z \neq 0, t = 0) = 0.0\,\mathrm{m\,s^{-1}}$ |
| Initial gas and solid temperatures | $T_f(x, y, t = 0) = 226.85°\mathrm{C}$<br>$T_s(x, y, t = 0) = 226.85°\mathrm{C}$ |
| Soild flow at top boundary | $v_s(r, z = L, t) = 0.0\,\mathrm{m\,s^{-1}}$ |
| Solid stress at top boundary | $\tau_s(r, z = L, t) = 0.0\,\mathrm{N\,m^{-2}}$ |
| Particle-particle restitution coefficient | $e_{pp} = 0.97$ |
| Wall-particle restitution coefficient | $e_{wp} = 0.90$ |
| Friction coefficient | $\bar{\mu} = 0.3$ |

**Table III.** Initial and boundary conditions applied into the numerical simulations

| Detector | z(cm) | r(cm) |
|---|---|---|
| 01 | 100.00 | 62.00 |
| 02 | 150.00 | 62.00 |
| 03 | 200.00 | 62.00 |
| 04 | 100.00 | 31.00 |
| 05 | 150.00 | 31.00 |
| 06 | 100.00 | 0.00 |

**Table IV.** Position of the six detectors within the bed. Detector 01 is at the bottom corner of the inner fluidized bed cavity

As helium gas at 60 bars pressure is pumped through the reactor and the bed expands and becomes supercritical, it heats up due to fission heat sources from neutrons. As the temperature of the particles increases the reactivity of the system decreases and eventually stabilizes in a time averaged sense, such that heat losses to the fluidizing helium balances the fission power. However, voidage oscillations in the reactor will provide a noisy fission-power.

*Temperature feedback and mixing*

The reactor has been designed to have an overall negative temperature coefficient. Which means that as the temperature increases the reactivity of the system decreases as shown in Figure 2(b). This provides a passive control of reactivity. This negative feedback effect makes the power respond very quickly to temperature changes in the reactor and enables this reactor concept to work (at least in the simulations) despite the rapid changes in reactivity of the system due to redistributions of the fuel particles in the reactor cavity.

It has been shown, in a previous study (Pain *et al.*, 2002b), that this mixing allows the particles to be exposed to the same fission-heat source over relatively small time scales (6 s of reactor operation at *quasi* steady-state). This means that the fuel will be uniformly burnt in the reactor. In that study it was also shown that despite the rapid variations in fission rate by an order of magnitude over as little as 1 s, the temperature of the reactor was remarkably steady and uniform. All these features have been observed also in this reactor and are thus not investigated in detail here.

*The central neutron transport theory simulation explained*

An axi-symmetric transient simulation was conducted using the mesh shown in Figure 1(a) and a $P_3$ (transport theory) angular expansion (three angular moments). A total fuel particle mass of 8429.28 g was used. Figures 3(a) and (b) show the fission rate and maximum temperature, respectively, of the reactor. The fission rate has a long-term oscillation associated with it as well as short-term oscillations. The long-term oscillations occur because the reactor is initially cool and thus the negative reactivity feedback effects associated with temperature take some time to take effect. This allows a large fission spike to develop which deposits a great deal of heat energy mostly in the bottom corner of the reactor and heats the system to a maximum temperature of 730°C, see Figure 3(b).

This rapid increase in temperature dissipates through the reactor, due to solids mixing and heat transfer through the gas phase. The result is a sharp initial pulse in maximum temperature, Figure 3(b), after which the bed temperature becomes quite homogeneous. However, it takes about 200 s for the fluidizing helium to extract enough heat energy from the particles for the system to become supercritical again and the fission rate to rise, see Figure 3(a). This is then followed by smaller but similarly produced subsequent oscillations.

It is well known that delayed neutrons in other nuclear reactors and critical systems (Pain *et al.*, 2001c) combined with heat losses also provide a mechanism for producing fission oscillations. A similar mechanism is believed to cause the longer fission power oscillations in this reactor. Graphs of the maximum longest lived delayed neutron precursor concentration, half life of 55 s, and the third longest lived delayed concentration, half life of 5 s, respectively, are shown in Figure 3. Figure 3(c) also

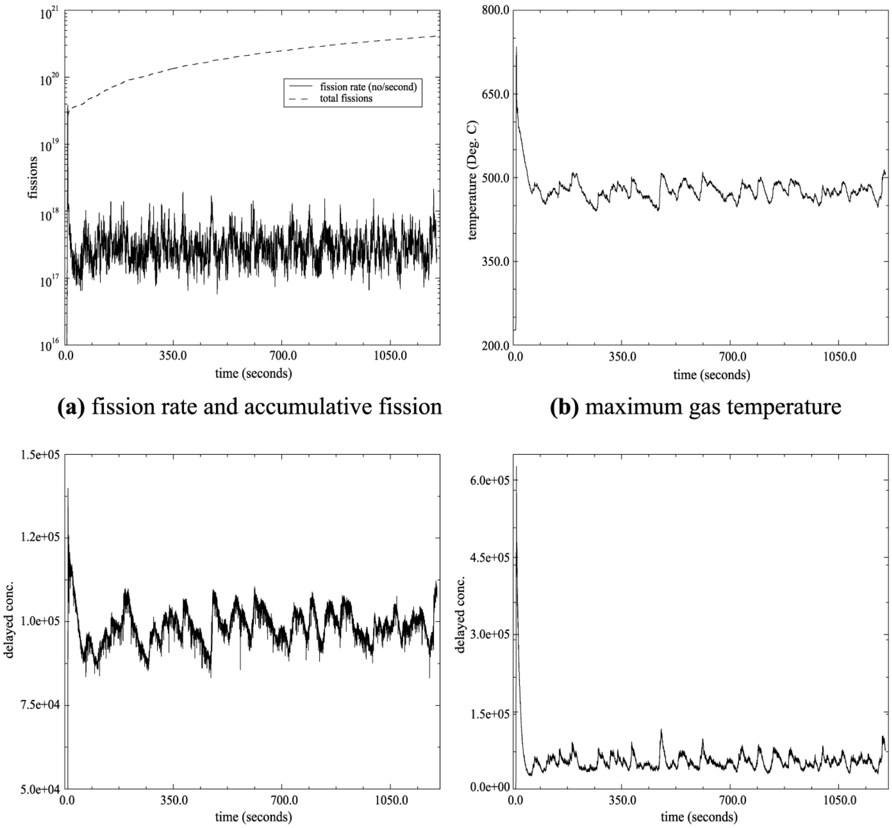


**(a)** fission rate and accumulative fission

**(b)** maximum gas temperature

**(c)** maximum longest lived delayed concentration

**(d)** maximum 3rd longest concentration

**Figure 3.** Time for the $P_3$ simulation conducted in *r-z* geometry

effectively shows the time averaged, over time scale of 55 s, heat source from fissions. Figure 3(d) shows the maximum delayed neutron concentration of the third longest lived group (half life of 6 s). The fission rate, solids volume fraction and gas temperature at the bottom corner (detector 1) of the reactor core are shown over a relatively short time period in Figure 4. Detector 1 is the detector at which the temperature varies most rapidly and thus this temperature gives an indication of the temperature range in the reactor.

*Fine mesh simulation*

In this section, the convergence in space of the simulated fluidized bed reactor is examined by dividing all elements in half in each direction. Therefore, there are four times the number of elements shown in Figure 1(a), i.e. there are 8,000 volume elements and 8,241 nodes. The fluids occupied domain has 3,000 volume elements and 3,171 nodes. In addition, a total fuel particle mass of 9046.06 g was used.

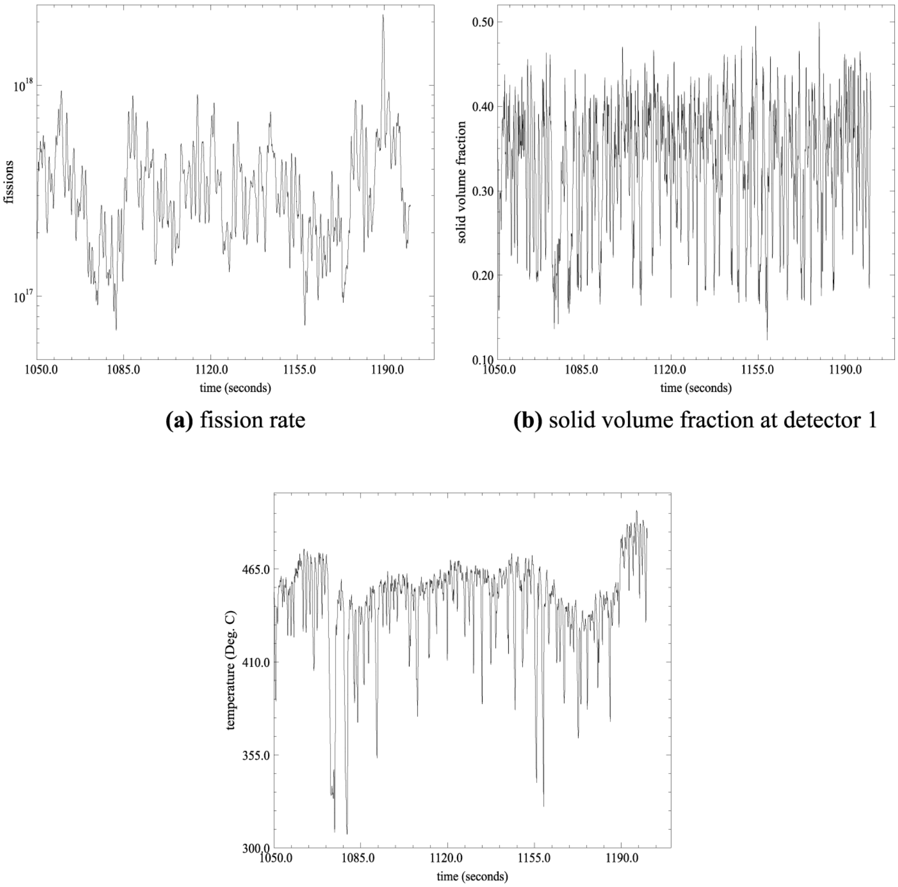


**(a)** fission rate

**(b)** solid volume fraction at detector 1

**(c)** solid temperature at detector 1

**Figure 4.**
(bottom corner of the reactor) *versus* time ($1,050 \leq t \leq 1,200\,\mathrm{s}$) for the $P_3$ simulation conducted in *r-z* geometry

This simulation was performed over 194 s using a $P_1$ neutron angle approximation and the fission rate and maximum gas phase temperature versus time for this short simulation (due to the computation expense) are shown in Figure 5. This does not have the large fission spike that most of the other simulations have. This highlights the rather unpredictable starting characteristics of this reactor with these extreme start up conditions. In addition, the solids temperature and particle volume fraction at detector 1 (bottom corner of reactor cavity) are shown in Figure 5(c) and (d). These figures are included to highlight the correlation between particle volume fraction at the bottom corner and power and, therefore, temperature of the reactor.

The volume fraction, solids temperature, 2nd longest lived delayed group and shortest lived delayed group fields are shown in Figure 6 at 80 s into this simulation. The similarity of the volume fraction and 2nd delayed groups has been noticed before, and is attributed to the fission heat source for each particle being the same when time averaged over the time scale of the half life of the 2nd delayed group which is 22 s. In addition, the shortest-lived delayed group, with a half-life of 0.2 s, reflects the power

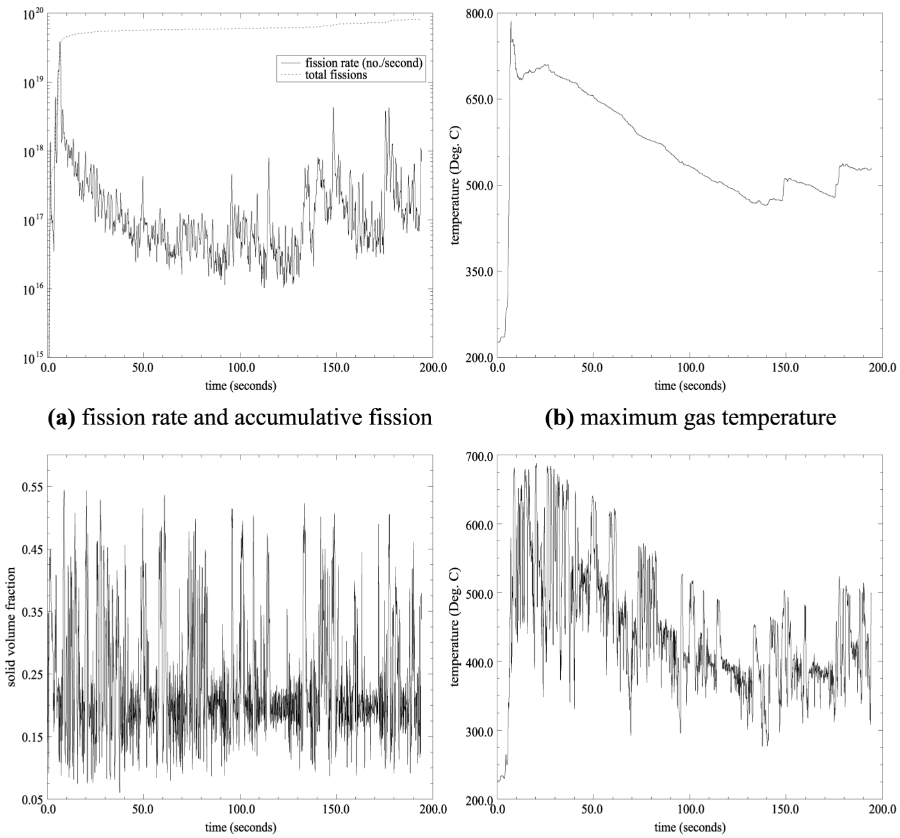


**(a)** fission rate and accumulative fission

**(b)** maximum gas temperature

**(c)** solid volume fraction

**(d)** solid phase temperature

**Notes:** Fluctuations of solid volume fraction (c) and solid phase temperature (d) obtained from detector 1 (Table IV) are also shown here

**Figure 5.**
Fission rate (a) and maximum gas temperature (b) *versus* time for the fine mesh simulation conducted in *r-z* geometry

distribution in the reactor at a given instance in time. As seen in Figure 6(d) the power is largest near the bottom corner of the internal cavity and next to the vertical walls. The walls are made from graphite which moderates and reflects the neutrons back into the reactor and coarsens subsequent fissions. Making the bottom of the 13 reactor from porous graphite has reduced the local effectiveness to reactivity of this area. Since the focus from this area of the reactivity is reduced and in some sense spread out, this has the effect of reducing the response to voidage fluctuations and is one of the main advantages of this new design. The solid volume fraction distribution at equally spaced time intervals between 80 and 82.5 s into the simulation, is shown in Figure 7. This is included to give an insight into the dynamics of this reactor. Correlations for bubble size and height at which slugs occur (Davidson *et al.*, 1985) suggest that the slugs would appear at about a 1.5 m height above the cavity floor. This is reflected in the results shown in Figure 7.

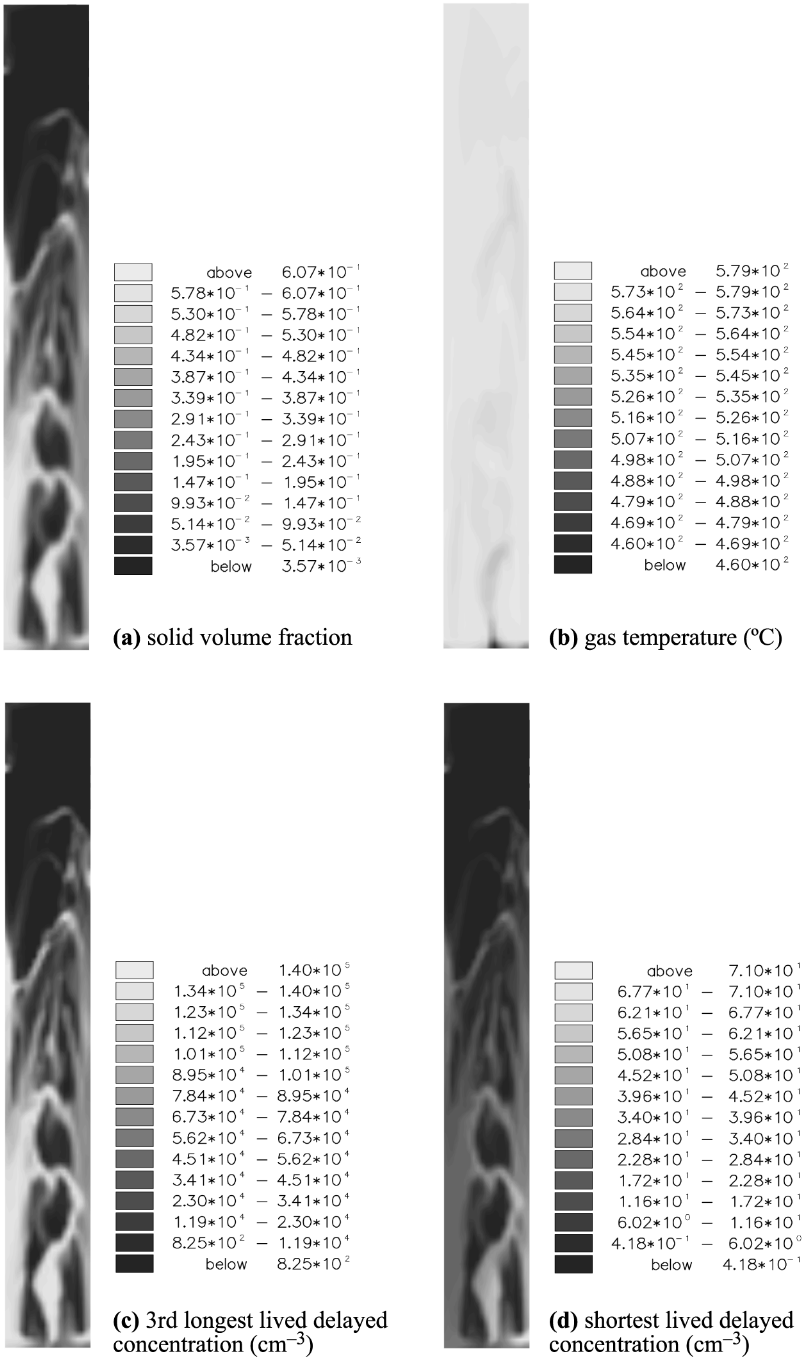


**(a)** solid volume fraction

**(b)** gas temperature (ºC)

**(c)** 3rd longest lived delayed concentration (cm$^{-3}$)

**(d)** shortest lived delayed concentration (cm$^{-3}$)

**Figure 6.**
Various fields at 80 s into the simulation with a fine mesh

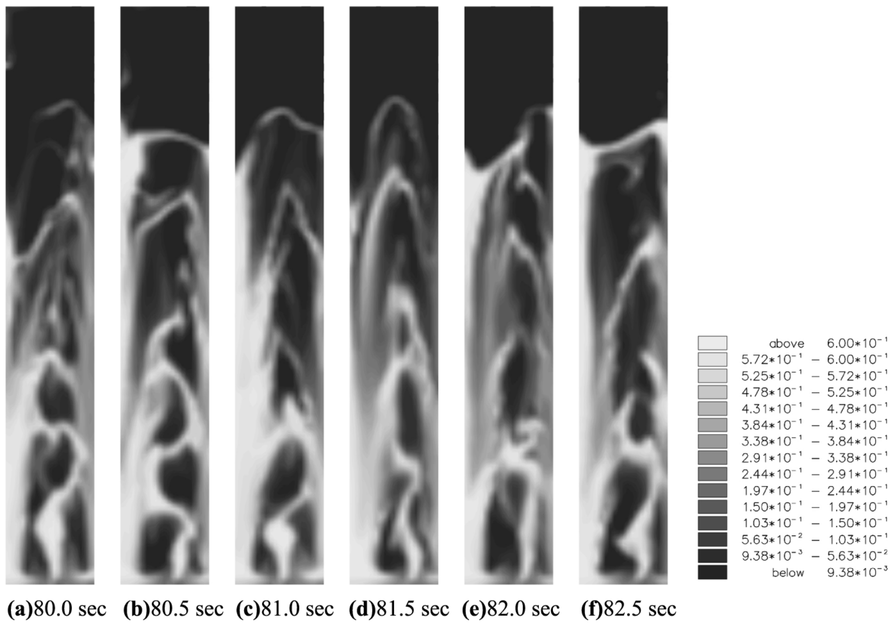


**Figure 7.**
The solid volume fraction at various time levels for the simulation with a fine mesh

*The effect of varying the gas fluidization velocity*

To investigate the effect of using a different inlet velocity, simulations with inlet superficial gas velocity of 60 and 120 cm/s were performed (the latter was used in all the other simulations). Figure 8 shows the fission rate and maximum solids temperature versus time of the simulation with the lower inlet gas velocity. This simulation was performed over a particularly long time of about 25 min because as can be seen in the fission rate curve this simulation was prone to producing large peaks in the fission rate, even after the initial conditions are no longer felt. The large peaks in the fission rate increases the temperature and makes the temperature vary by as much as 100°C. Notice that the temperature of this reactor is nearly as large (in a time average sense after the initial pulse) as the temperature of the same simulation but with a larger inlet velocity. This is due to the flatness of the $K_{\text{eff}}$ versus expanded height curve. The fluidized bed has expanded to about a height of 2.25 m, and thus will produce a temperature near that of the bed with 120 cm/s inlet velocity which expanded the bed to approximately 4 m in height.

There are some similarities in temperature between this simulation and the simulation conducted at 120 cm/s gas inlet velocity. This means that the quantity of gas heated is half of the simulation conducted with an inlet gas velocity of 120 cm/s. Therefore, the fission rate produced from the simulation with lower inlet gas velocity is approximately half of the simulation performed with a larger inlet gas velocity as shown in Figures 8(a) and 9(a) (Table V).

In order to investigate the reactor response to variable inlet velocity and also the reproducibility of this response, a simulation was performed with a sinusoidal varying gas inlet velocity. The period of this oscillation is 720 s and has a minimum and

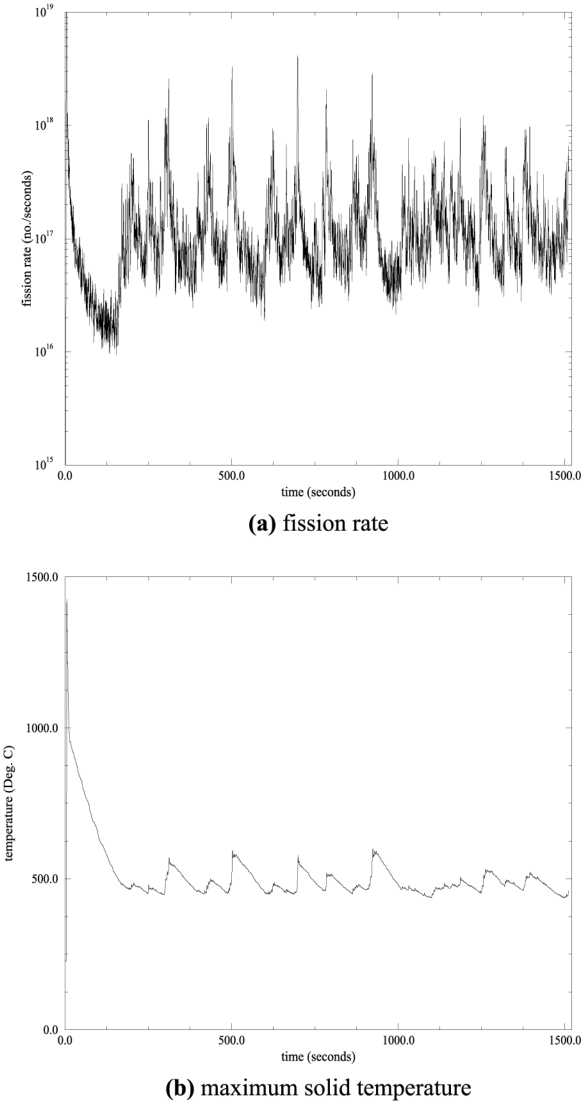


**Figure 8.**
Time for the $P_1$ simulation conducted with a relatively low inlet velocity and in *r-z* geometry

maximum velocity of $-120$ cm/s (outgoing velocity) and 120 cm/s, respectively. The velocity starts from zero and increases to its maximum which occurs at 180 s. Figure 10 shows the resulting fission rate and maximum temperature versus time for this simulation. Notice that the fission rate starts to increase rapidly at about 50 s into the simulation and reaches a peak shortly after this when the inlet gas velocity is about 51 cm/s. Much of the next 150 s are taken up by draining the large quantity of heat energy thus deposited out of the system. The fluidizing gas velocity starts to decrease at 180 s into the simulation and eventually reaches the stage when it no-longer fluidized the particles. This is seen in the smoothness of the fission rate variation. The fission

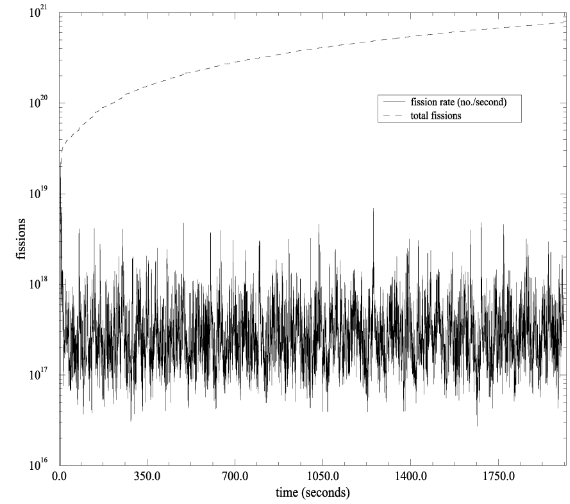


**(a)** fission rate and accumulative fission

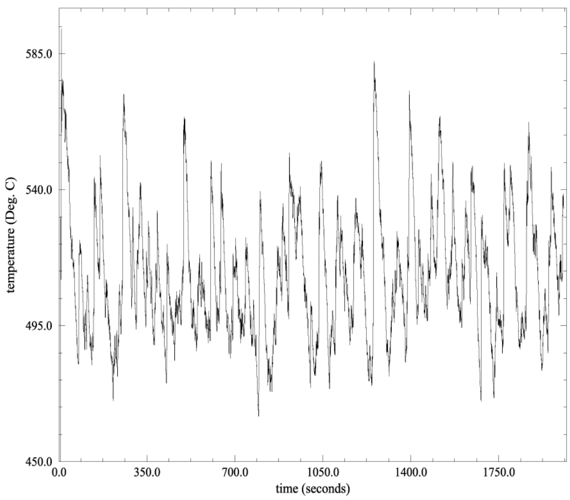


**(b)** maximum gas temperature

**Figure 9.**
Time for the $P_1$ simulation conducted in *r-z* geometry with an inlet gas velocity of 120.0 cm s$^{-1}$

| Simulation | Length of the time-window (s) | Power (MW-thermal) |
|---|---|---|
| $P_3$ | 1003.35 | 10.41 |
| $P_1$ | 1809.62 | 12.00 |
| $P_1$-fine mesh simulation | 194.18 | 4.20 |
| $P_1$-low inlet gas velocity | 1311.22 | 5.46 |

**Notes:** Power output of the 2D simulations performed in this work. The power outputs listed here are calculated after stationarity was reached in the numerical simulation

**Table V.**

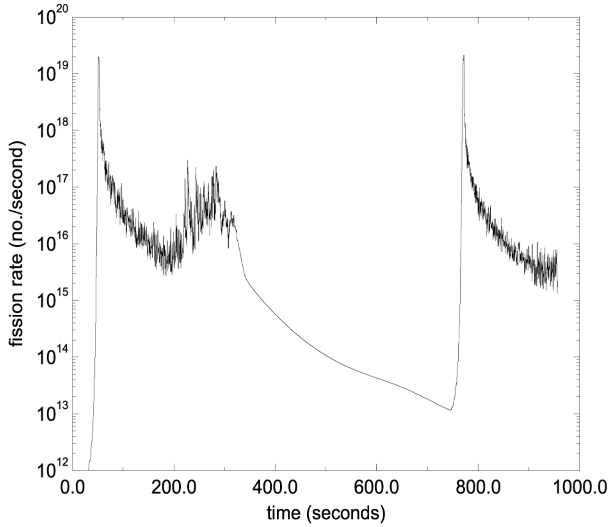


**(a)** fission rate

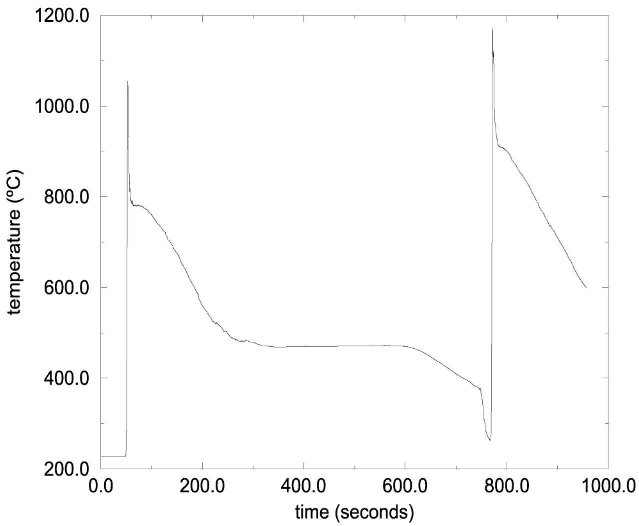


**(b)** maximum particle temperature

**Figure 10.**
Time for the simulation conducted with a sinusoidal inlet velocity and in *r-z* geometry

rate starts to decrease because of the combined effectivity of the negative temperature coefficient and the collapsed bed start (geometry of smallest reactivity). It continues decreasing despite the fact that the negative gas velocity eventually brings cool helium at 220°C from above to cool the particles. The particles are sufficiently cooled by this gas that once the gas velocity at the distributor become positive again and the particles fluidized, the fission rate repeats the large peak and in fact will carry on repeating this whole cycle. The 2nd 15 fission peak occurs again at about 50 s into the second cycle.

The time averaged solid volume fraction for the four simulations with constant gas inlet velocity is shown in Figure 11. Notice that as well as the particle concentration being relatively large at the vertical walls it is also large near the central axis. However, this is not consistent with experimental results observed in similar geometries and

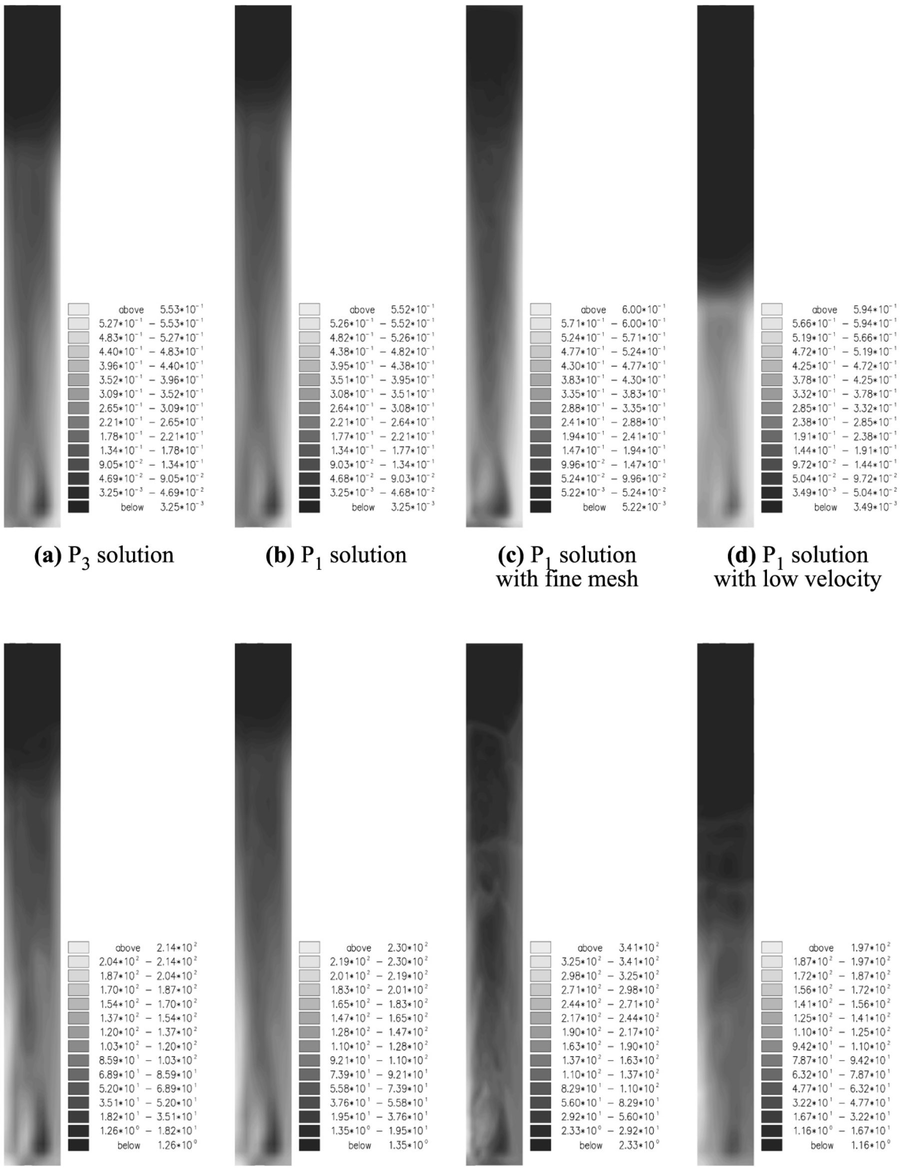


**(a)** $P_3$ solution **(b)** $P_1$ solution **(c)** $P_1$ solution with fine mesh **(d)** $P_1$ solution with low velocity

**(e)** $P_3$ solution **(f)** $P_1$ solution **(g)** $P_1$ solution with fine mesh **(h)** $P_1$ solution with low velocity

**Figure 11.**
Time averaged solid volume fraction (a-d) and shortest lived delayed neutron precursor concentrations (e-h) for the four different simulations

with similar particle sizes and densities (Davidson *et al.*, 1985). This discrepancy is probably due to superimposing axi-symmetry on the flow. This has provided the motivation for conducting 3D simulations. The time averaged shortest lived delayed neutron precursor concentration which reflects the particle time averaged power distribution is also shown in Figure 11(e)-(h).

*Reactors performance*

Table V shows the power output of the simulations described in the previous sections. The power outputs shown in this table were calculated after stationarity was reached, therefore, any energy spike obtained from the transient was neglected. The simulation performed with a low inlet gas velocity produced approximately half of the energy produced by the simulation performed with twice the inlet gas velocity as explained in the previous section. The $P_1$ and $P_3$ simulations produced nearly the same amount of energy, 12.00 and 10.41 MWt, respectively.

## 3D Numerical simulation results

The 3D simulation conducted here had a total of 24,288 volume elements and 25,991 nodes as shown in Figure 12. The fluids calculation domain had 12,096 elements and 13,357 nodes. It was performed over 22 s real time and took approximately 22 days of CPU time, on a Compaq ES40 workstation with four 833 MHz alpha processors and 512 Mb of shared memory.

The initial and boundary conditions applied to this simulation are similar to those applied to the *r-z* geometry, which are summarized in Table III, except that the total amount of fuel now is 1,987 kg and the inlet flow rate is 120.0 cm s$^{-1}$.

The fission rate and maximum temperature in the reactor for this simulation are shown in Figure 13(a) and (b), respectively. The fission rate becomes large enough to start heating the solution at, approximately, 18 s into the simulation. The solids volume fraction and temperature at detector 1 (situated at the bottom corner of the internal cavity) are shown in Figure 13(c) and (d), respectively.

Various time averaged fields are displayed on a plane along the center of the reactor in Figure 14. As shown in time-averaged solid phase velocity, Figure 14(d), the particles, in a time-averaged sense, fall in the wall region and rise in the center of the reactor.

Various other fields at 20 s into the simulation are shown in Figure 15. In this figure it is seen that the gas moves preferentially through the bubbles and that the granular temperature is largest in the wake region of bubbles.

## Dynamic analysis

Despite the extensive efforts to improve the results obtained from numerical simulations by the development of new numerical techniques, comparisons of such results and those obtained from experiments are still an issue, since only statistical quantities can be properly compared (Bai *et al.*, 1997; Huilin *et al.*, 1995; van der Stappen *et al.*, 1993). As the granular flow in fluidized beds are chaotic, dynamic analysis has been applied to time series of either voidage or pressure fluctuations to identify flow regime (e.g. bubbling and slugging bed).

Some noteworthy reviews and fundamentals of chaos theory can be found in Anishchenko (1995) (Johnsson *et al.*, 2000). One of the first works published on chaos

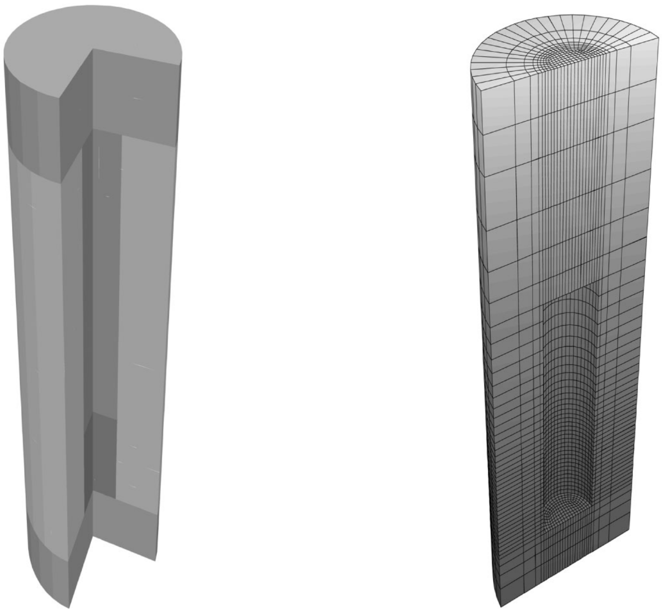

**(a)** 3-D schematic of the fluidized bed reactor **(b)** 3-D finite element mesh

**Notes:** Half the 3-D mesh is shown here without the internal fluid solution domian. The 1 meter of plenum above this is occupied by helium gas

**Figure 12.**
Nuclear fluidized bed reactor: (a) Schematic and (b) finite element mesh

theory applied to fluidized beds is due to Baskakov *et al.* (1986), who associated pressure fluctuations with bubbles flowing around pressure transducers. Huilin *et al.* (1995) used pressure fluctuation data, obtained from a lab-scale circulated fluidized bed (CFB), to calculate the correlation dimension, which can be defined as a measure of the spatial homogeneity of an attractor. They used the correlation dimension to infer *real dimensionality* of a system and to establish the number of differential equations that are needed to describe a system. They also used Lyaponov exponents to determine how chaotic different fluidization regimes are.

Dynamic systems that display a chaotic behavior, can only be analyzed through statistical methods. The set of differential equations used to describe such systems are time-dependent, however, after a period of time, the solution tends to become time-independent, i.e. reaches stationarity. Once stationarity is reached, statistical analysis can be performed. Indeed, many researchers have addressed the issue of establishing a stationary point, from which statistical analysis can be performed.

In this section, the results obtained from the numerical simulations were analyzed through deterministic chaos theory. In order to identify flow regime, some statistical parameters, such as power spectra density, correlation dimension and Kolmogorov entropy, were obtained from voidage and fission-power time series. Reviews about dynamic analysis can be found in Anishchenko (1995) and in Yaffee and McGee (2000). As the numerical simulations performed in complex geometries are very computational demanding, a surrogate method based on a simplified Kriging

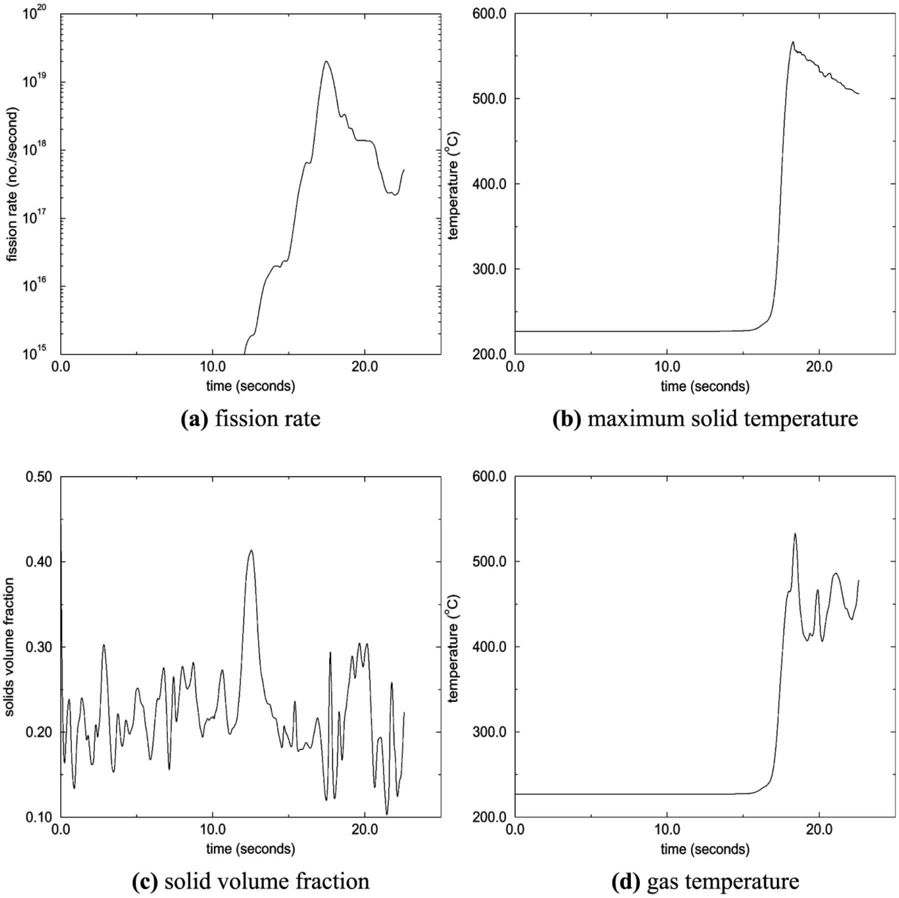


**Figure 13.**
Time for the simulation conducted with 3D geometry. Oscillations of solid volume fraction (c) and gas phase temperature (d) obtained from a detector placed in the bottom corner of the internal cavity

technique was applied to fission-power time series in order to predict, in a short-time sense, the fission-power behavior. Therefore, some variables, such as fission-power, pressure or temperature, could be monitored and used to provide short-term predictions. These predictions might be used in the fluidized bed nuclear reactor to provide control.

*Testing for stationarity*
Stationarity is defined as a property in which the mean and the variance of a given time series do not change over a period of time. This means that the dynamic properties of the systems underlying signal must not change during that period of time, and over short-time intervals, the variance should not vary significantly (Yu *et al.*, 1998).

Stationarity can be classified into weak stationarity, which has a constant mean and variance, and strongly stationarity, which has all higher-order moments constant. Although strongly stationarity is considered to be genuine stationarity, it is hardly seen in practice (Kantz and Schreiber, 2002).

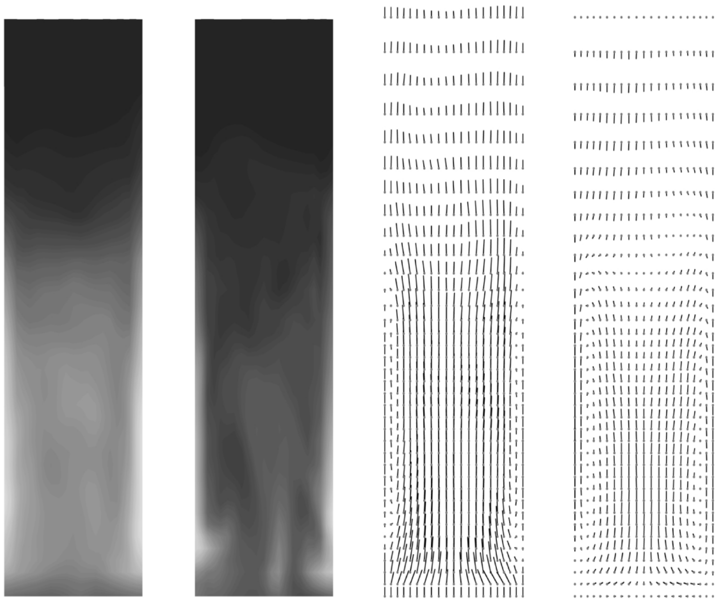

(a) (b) (c) (d)

**Notes:** The fields were time-averaged over 22 seconds. The maximum velocity shown in (c) and (d) are 390 and 237 cm/s, respectively

**Figure 14.** 3D simulation: various time-averaged fields drawn on a plane along the centre of the reactor: (a) solid volume fraction; (b) 6th delayed group; (c) gas phase velocity and (d) solid phase velocity

Several statistical tests for stationarity have been proposed in the literature (Yu *et al.*, 1998; Kantz and Schreiber, 2002); in most of these tests a parameter (for example, power spectrum, mean or variance) is estimated using different segments of the time series. The set of parameters are evaluated and if the variation among them is significant, i.e. beyond an estimated deviation, the time series is assumed to be nonstationary. Kennel (1997), however, used the information obtained from time distribution of points in a state space to infer stationarity. His method investigates the geometry of orbits in state space by quantifying nonstationarity from the properties of nearest neighbors in state space. Schreiber (1997) tested for stationarity by checking for compatibility of nonlinear approximations to the dynamics in different segments of the time series. Casdagli (1997) made a brief review of recurrence plotting techniques to detect nonstationarity in nonlinear time series.

In this work, the power spectra density of several fragments of data of fission rate and voidage fluctuations were calculated. The dominant frequency and overall behavior of the set of PSD's were compared, and if no large shift to any side was found, the dynamics were assumed to have reached stationarity. The PSD's of fission rate fluctuations of the $P_1$ simulations are shown in Figure 16. From the original time series ($\Delta t = 2,010\,\mathrm{s}$), the first 500.0 s were discarded, and the remaining time series investigated. In Figure 16(a), the PSD of 1510.0 s of numerical simulation is plotted and a dominant frequency between 0.25 and 0.375 is observed. Similar dominant frequencies can be observed using different segments of data, Figure 16(b)-(d),

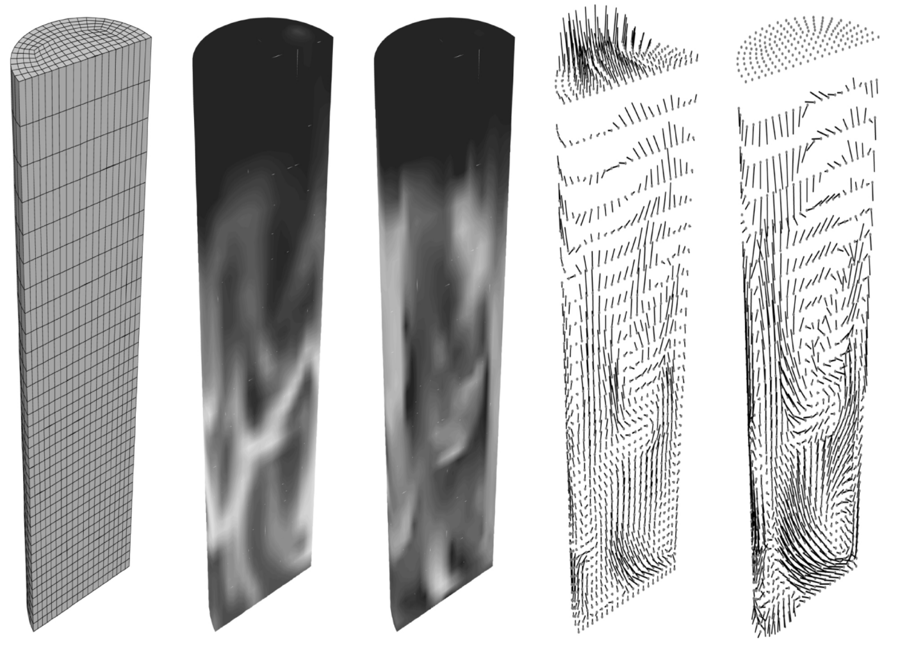


**Figure 15.**
Various fields at 20 s into the 3D simulation shown on half the domain

indicating that the time series has reached stationarity. This test was applied to all time series obtained from numerical simulations described in this work, and all analysis were conducted at stationarity.

*Bubble production and fission-power coupling*

In fluidized beds operating in bubbling regimes, bubbles are formed in the bottom region, i.e. in the vicinities of the distributor, and as they rise in the center region, particles are dragged in their wake creating strong vortices (Buyevich *et al.*, 1995). In the edges of the bubbles, regions of low solid volume fraction, act as shells around the bubbles. In such shells, the granular temperature (particle agitation) is enhanced due to both the increasing of the mean free path between particles and the increasing in collision frequency. As bubbles rise upwards through the bed, the bubbles, eventually coalesce, producing larger bubbles which are released in the free board, dragging particles in their wake, (Pain *et al.*, 2002a). In this train of rising bubbles, particles are replaced in the bubbles' wake enhancing the heat transfer rate. Simultaneously, particles fall, preferentially in the wall region, as shown in Figure 14(d). Once these particles get near the distributor they change directions due to the rising bubbles. Such flow reorientation was previously reported by van der Stappen *et al.* (1993).

In the simulations described in this work, although the overall dynamics are very similar to those described in the literature (Davidson *et al.*, 1985; Pain *et al.*, 2002a), the

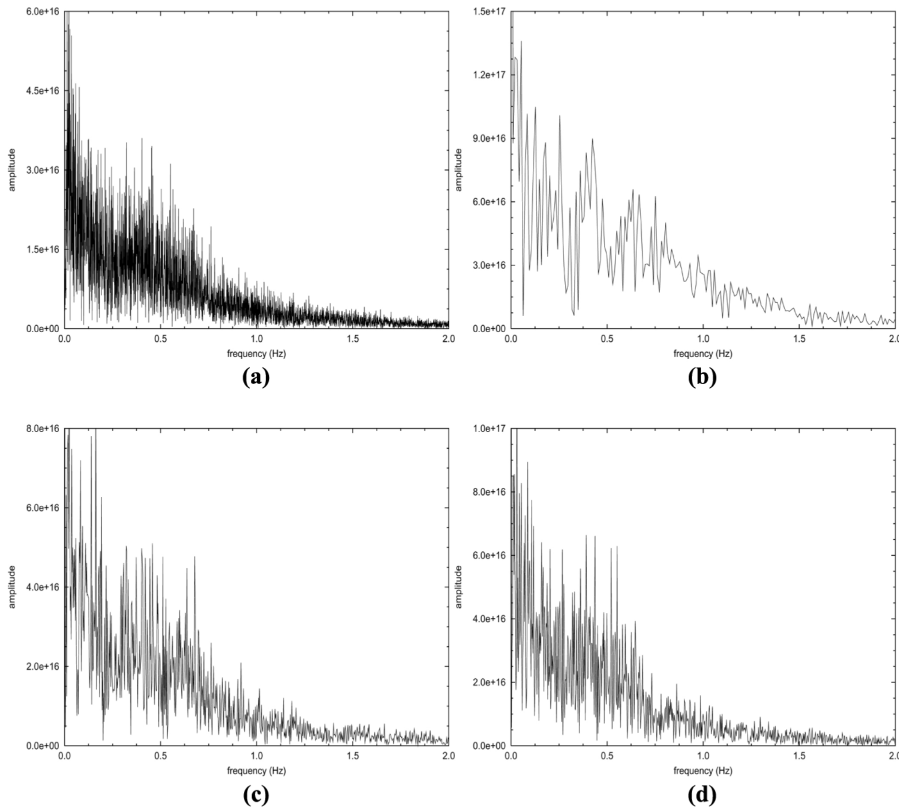


**Notes:** As the first 500 seconds were neglected, the further 1512 seconds were tested for nonstationarity by comparing the fission rate power spectra density of several segments of data through the time series: (a) all data, (b) $0.0 \leq t \leq 94.50$ seconds, (c) $775.0 \leq t \leq 1153.0$ seconds and (d) $1134.0 \leq t \leq 1512.0$ seconds

**Figure 16.**
Stationarity test of the $P_1$ simulation

releasing of fission-power, due to the reactivity, followed by bed expansion, add an important variable in the investigation of the balance of forces acting during fluidization. In order to investigate the bubbles formation, mainly in the bottom region, the power spectra density of voidage and fission rate fluctuations were calculated. Figure 17 shows the PSD of voidage fluctuations obtained from the six detectors during the $P_3$ simulation. Lower dominant frequencies were obtained from the detectors placed some distance from the distributor, i.e. detectors 2, 3 and 5. At these detectors, the dominant frequency is approximately 0.40 Hz, although detector 5 has a second peak at 0.60 Hz. Detectors 1, 4 and 6 (in the bottom region) have similar dominant frequencies between 0.65 and 0.70 Hz. The PSD obtained from the fission rate fluctuations of the $P_3$ simulation, Figure 18(a), shows two major dominant frequency ranges, the first around 0.5 Hz and the second in the range between 0.60 and 0.70 Hz, which matches with the dominant frequencies found in Figure 17.

The PSD of fission rate fluctuations for the central $P_3$ and the $P_1$ simulations are shown in Figure 18. In all simulations, dominant frequencies between 0.50 and 0.75

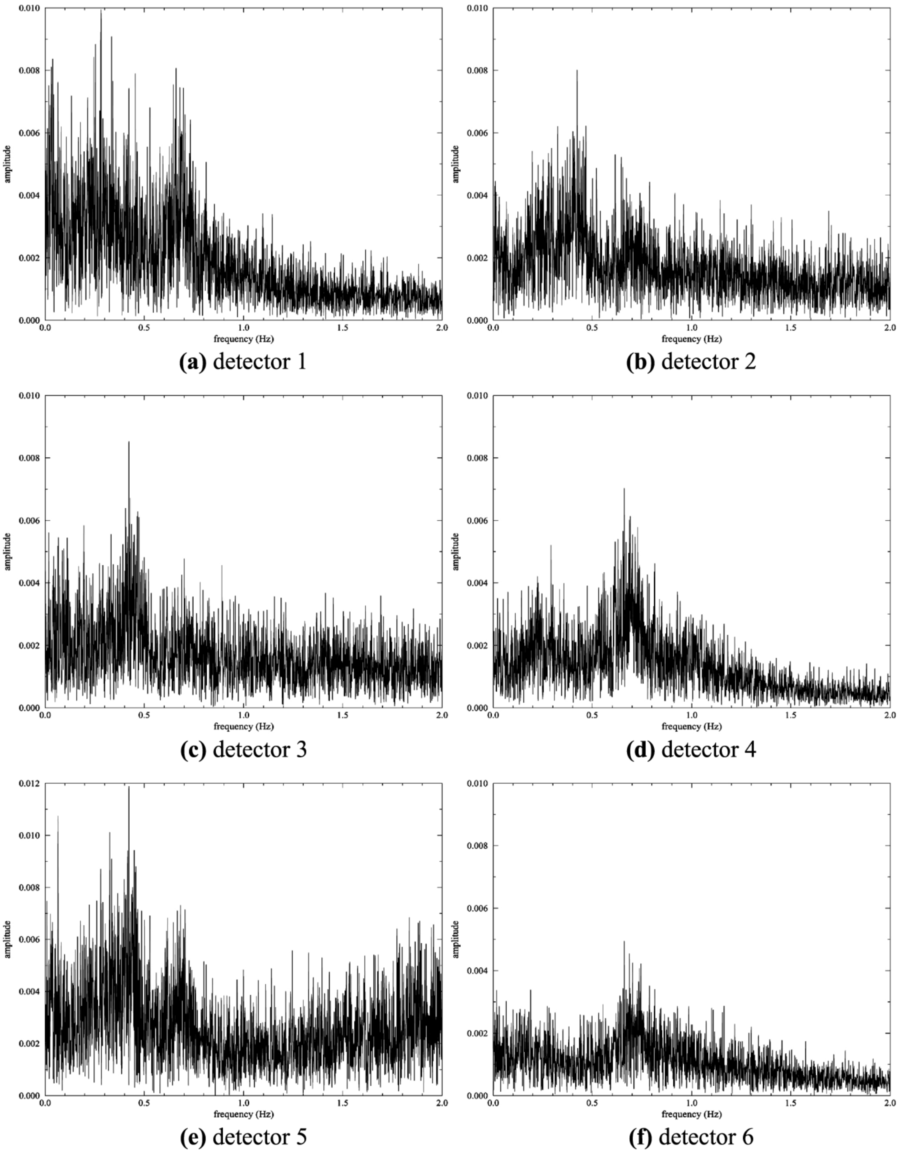


**Figure 17.**
Power spectra of voidage fluctuations at the six detectors (Table IV) in the $P_3$ simulations

were found, and a similar amplitude range can be seen, except for the $P_1$ simulation performed with a fine mesh which has larger amplitudes. This is probably due to the fact that there is not enough data, after the system has reached stationarity, to compute the PSD. As shown by Figures 18(a) and 17(a), (d) and (f), there seems to be a strong link between the particle concentration fluctuations at the bottom region of the reactor and the fission power, with the same dominant frequency of 0.7 Hz. The PSD of

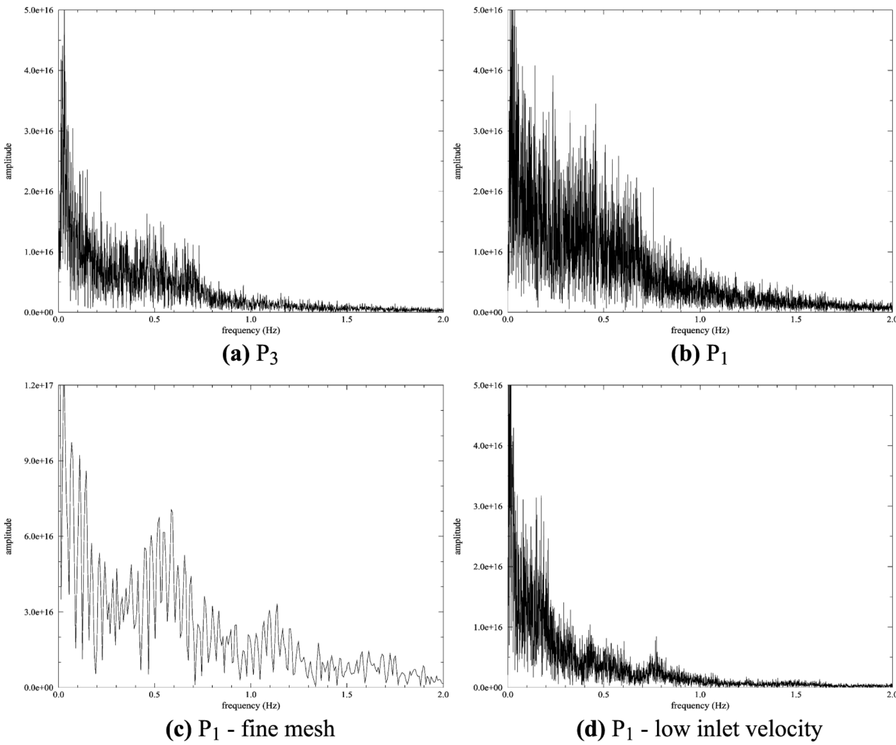


**Figure 18.**
Power spectra of fission rate fluctuations for the four simulations conducted in this work

voidage fluctuations obtained from the four simulations at detector 1 (bottom corner) are shown in Figure 19.

As the fission rate production and solid volume fraction fluctuations are related through the geometrical dependence of reactivity of the reactor, the cross correlation function (CCF) was used to calculate the time-lag between these time series. The CCF is defined as a measure of the similarity between two different data sets: the input and output time series. It is computed as the covariance between the input and output time series divided by the product of the standard deviation of both time series:

$$\mathrm{CCF} = \begin{cases} \dfrac{\sum_{t=1}^{n+j} (X_{t-j} - \overline{X})(Y_t - \overline{Y})}{\sqrt{\sum_{t=1}^{n} (Y_t - \overline{Y})^2}\sqrt{\sum_{t=1}^{n} (X_t - \overline{X})^2}} & \text{if } j \leq 0 \\[2ex] \dfrac{\sum_{t=1}^{n+j} (X_t - \overline{X})(Y_{t+j} - \overline{Y})}{\sqrt{\sum_{t=1}^{n} (Y_t - \overline{Y})^2}\sqrt{\sum_{t=1}^{n} (X_t - \overline{X})^2}} & \text{if } j > 0 \end{cases} \tag{1}$$

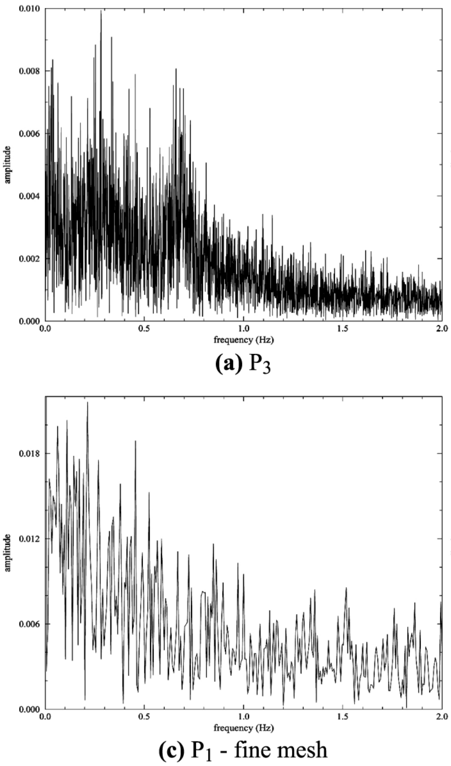


**Figure 19.**
Power spectra of voidage fluctuations at detector 1 (in the bottom corner of the bed) for the four simulations

where $X$ and $Y$ are the input signal and response, respectively. $n$ and $j$ are the number of sample points and the lag of cross-correlation, respectively. Significant positive spikes in the cross-correlation function indicate that the input variable variations lead the corresponding variations in the output variable. However, significant negative spikes indicate possible feedback from the output to the input variables (Yaffee and McGee, 2000). The CCF indicates the transfer function direction between the time series and delay between input and output. Indeed, after some delay $\Delta t$, if the CCF is positive, then $X_t$ is correlated after some delay $\Delta t$ with $Y_{t+\Delta t}$. Figure 20 shows the cross correlation calculated between solid volume fraction and fission rate fluctuations at six detectors (Table IV) in the $P_3$ simulations. Shorter time delays were found in detectors 2 and 3. Figure 20(b) shows that approximately 0.19 s after an increase in solid volume fraction, there is an increase in power. As large bubbles rise from the wall region, they travel upwards through the reactor, generating particle concentration waves. Such waves are responsible for negative time-delays as shown in detectors 1 and 5. In addition, several negatives peaks can be noticed, indicating a reaction feedback from the power released from the formation of bubbles.

*Study of the flow regime and macrostructure through dynamics analysis*

In this section two statistical parameters: maximum-likelihood estimations of the correlation dimension ($D_{ML}$) and the Kolmogorov entropy ($K_{ML}$) are used to help

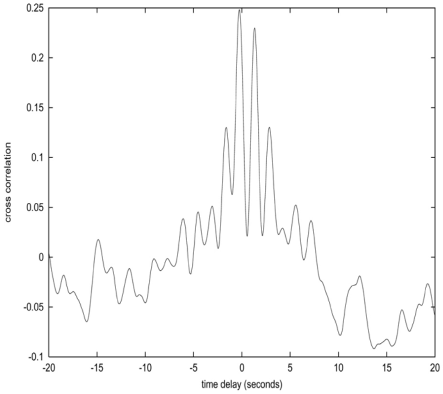


**(a)** detector 1 (-0.28/1.29 sec)

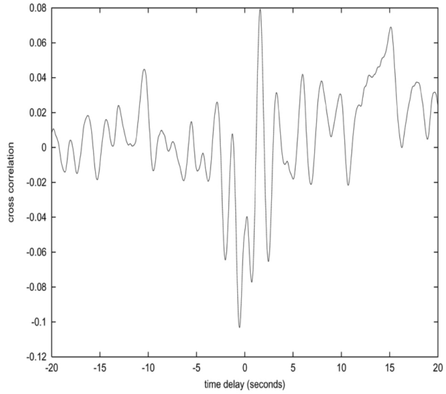


**(b)** detector 2 (-1.28/0.19 sec)

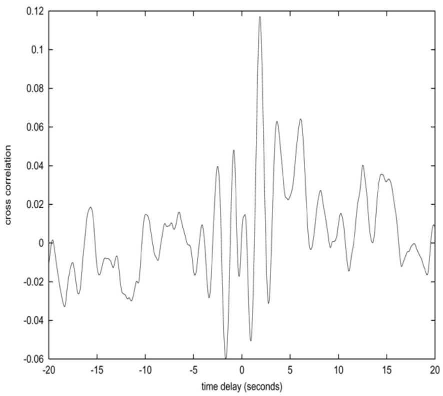


**(c)** detector 3 (-0.87/0.27 sec)

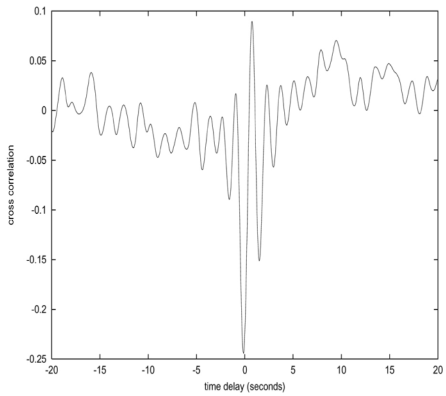


**(d)** detector 4 (-0.93/0.73 sec)

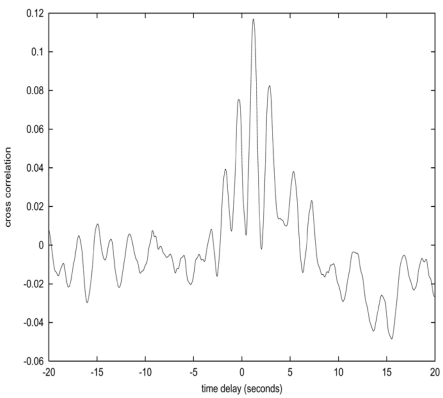


**(e)** detector 5 (-0.32/1.18 sec)

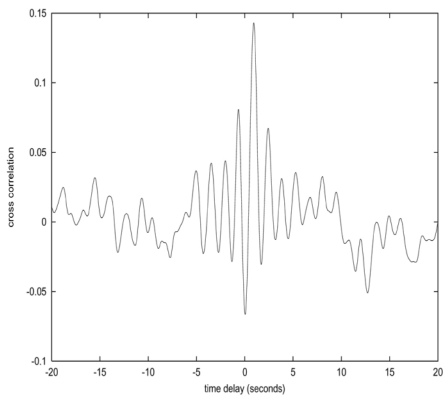


**(f)** detector 6 (-0.66/0.91 sec)

**Notes:** The first and second number in the brackets represent the positive and negative time-lag associated with the peaks in cross-correlation nearest the zero time delay

**Figure 20.**
Cross correlation of solid volume fraction and fission rate fluctuations at four detectors (Table IV) in $P_3$ simulations

investigating the chaotic behavior of simulated gas-solid fluidized beds. These parameters (Johnsson *et al.*, 2000; Pain *et al.*, 2002a) were calculated by the means of the RRCHAOS software package (Schouten and van der Bleek, 1993).

The correlation dimension ($D_l$) estimates the average number of data points within a radius $r$ of the data point. Indeed, the correlation dimension can be defined as a measure of the spatial homogeneity in the state space and it is obtained from the correlation integral, $C(l)$, which is defined as the probability that two points on the attractor are within a cell of size $l$ (Grassberger-Procaccia method – Grassberger and Proccaccia, 1983a):

$$C(l) = \frac{1}{N(N-1)} \sum_{j=1}^{N} \sum_{i=1, i \neq j}^{N} \Theta(l - \|\underline{x}_i - \underline{x}_j\|) \tag{2}$$

where $\underline{x}_i$ and $\underline{x}_j$ are the pair of points on the attractor whose distance is smaller than $l$, $N$ is the number of points, $\Theta$ is the Heaviside step function defined as:

$$\Theta(\mu) = \begin{cases} 1 & \text{for } \mu \geq 0 \\ 0 & \text{for } \mu < 0. \end{cases} \tag{3}$$

$\|\underline{x}_i - \underline{x}_j\|$ is the distance between two points in the attractor. For small length scales, the correlation integral and the correlation dimension, $D_l$, are related (Anishchenko, 1995):

$$C(l) \approx l^{D_l}. \tag{4}$$

Schouten *et al.* (1994a) suggested the following expression for the maximum-likelihood estimation of the correlation dimension ($D_{\mathrm{ML}}$):

$$D_{\mathrm{ML}} = -\left[\frac{1}{M} \sum_{i=1}^{M} \ln\left(\frac{l_i}{l_0}\right)\right]^{-1} \tag{5}$$

where $M$ is the sample size of interpoint normalized distances $r_i = l_i/l_0$. The distances $l_i$ are normalized by the maximum scaling distance, $l_0$.

The Kolmogorov entropy can be defined as the sum of the positive Lyapunov exponents of chaotic systems. Indeed, it is a measure of the rate of information loss along the attractor, i.e. a measure of the degree of predictability of points along the attractor given an arbitrary point (Schouten *et al.*, 1994b). Thus, the Kolmogorov entropy might be used to characterize the time dependent behavior of fluidized beds (van der Stappen *et al.*, 1993).

The basic idea behind the Kolmogorov entropy is the average time required for two orbits of the attractor, which are initially very close, to diverge. Thus, let us define two points on the attractor which are, initially, within a maximum distance $l_0$. Grassberger and Proccaccia (1983b) suggested that the separation of nearby points are exponential and the time interval, $t$ needed to separate such points by a distance larger than $l_0$ are exponentially distributed as

$$C(t) \approx e^{-Kt}$$

where $K$ is the Kolmogorov entropy. For constant time intervals, $t_0 = 1/f_{\mathrm{s}}$, a discrete distribution function may be defined as:

$$C(b) = e^{-Kbt_0} \quad \forall \;\; b = 1, 2, 3, \ldots \tag{6}$$

$b$ is the number of sequential pairs of points on the attractor, given an initial pair of independent points within a distance $l_0$, in which the interpoint distance is, for the first time, larger than $l_0$.

The normalized probability density function of finding a distance larger than $l_0$ after exactly $b$ interpoint distances is expressed as (Schouten and van der Bleek, 1993):

$$\sum_{b=1}^{\infty} p(b) = (e^{Kt_0 b} - 1) \sum_{b-1}^{\infty} e^{-Kt_0 b} = 1 \tag{7}$$

Thus, the probability of finding the exactly sample $(b_1, b_2, \ldots b_M)$, depending on $Kt_0$, from $M$ random pairs of independent points on the attractor is

$$p(Kt_0) = p(b_1, b_2, \ldots, b_M; Kt_0) = \prod_{i=1}^{M} p(b_i; Kt_0) = (e^{Kt_0} - 1)^M e^{-M \sum_{i=1}^{M} b_i} \tag{8}$$

The maximum of this function leads to the maximum-likelihood estimation of the Kolmogorov entropy, $K_{\mathrm{ML}}$, (Schouten *et al.*, 1994b)

$$K_{\mathrm{ML}} = -f_{\mathrm{s}} \ln\left(1 - \frac{1}{\bar{b}}\right) \tag{9}$$

with

$$\bar{b} = \frac{1}{M} \sum_{i=1}^{M} b_i \tag{10}$$

where $\bar{b}$ is the average value of the set of $b_i(\forall_i = \{1, 2, \ldots, M\})$ in the sample of size $M$, and $f_{\mathrm{s}}$ is the sampling frequency. $K_{\mathrm{ML}}$ is measured either as bits/*s* or as bits/cycle, which are related to the loss of information in real time units and within an average cycle in the time series, respectively (Schouten *et al.*, 1994b).

These parameters must be used together with the power spectra density to characterize fluidization regime and fluid flow macrostructure. Johnsson *et al.* (2000) studied gas-solid fluidization regimes by investigating pressure time series. According to them, for low and high velocities slugging regimes, the $D_{\mathrm{ML}}$ should be around 2.0 and 6.0, respectively, whereas for bubbling regimes, the maximum-likelihood estimation of the correlation dimension should be around 5.0. The $D_{\mathrm{ML}}$ obtained from voidage fluctuations, shown in Table VI, indicates that the flow oscillates from bubbling to the high-velocity slugging regime. Such oscillation is mainly due to the transient flow characteristic and may be observed in the set of diagrams shown in Figure 21.

The maximum-likelihood estimation of the Kolmogorov entropy is strongly related to the macrostructure of the flow, therefore, it may be used to characterize the complexity of the flow regimes. Pain *et al.* (2002a) reported that the $K_{\mathrm{ML}}$ varies with detector position, i.e. $K_{\mathrm{ML}}$ increases with the increasing of detector's distance from the distributor. Such behavior, due to bubbles formation and recirculation of particles, can be observed in Table VII.

*Flow regime characterization*

The TRISO coated particles used in the simulations performed in this work belongs to group D of Geldart's classification of powders. Although such powders may be easily spouted, fully bubbling and slugging regimes may also be found and the transition between these flow regimes is not easily distinguished.

Bayens and Geldart (1974) classified the slug behavior in two major types: round-nose and square-nose. Round-nose slugs are fast-bubbles usually associated with the fluidization of powders of group A. They are characterized by downflow of particles with a rising slug and a gas emulsion interface. In addition, the slug rise velocity is larger than the gas velocity. The square-nose slug, however, may be characterized by coarse particles been fluidized by large gas velocities. The slug rise velocity here is lower than the gas velocity and there is no clear slug boundary as shown in the set of diagrams in Figure 21. In these diagrams, in which solid volume fraction of the $P_1$ simulation evolves in time, the fluidized bed reactor oscillates from fully bubbling to the slugging regime.

Several empirical correlations have been suggested to predict many parameters associated with transient bubbling-slugging beds such as minimum slugging velocity, mean bubble diameter, maximum bed height, single slug velocity and slugging frequency (Noordergraaf *et al.*, 1987; Davidson *et al.*, 1985). Some of these parameters are investigated here.

Stewart and Davidson (1967) suggested that at the onset of slugging

$$\phi = \frac{U - U_{\mathrm{mf}}}{0.35\sqrt{gD}} \geq 0.2 \tag{11}$$

where $U_{\mathrm{mf}}$ and $D$ are the minimum fluidization velocity and the bed diameter. $U$ is the superficial velocity, corrected at the time-averaged temperature. The minimum slugging velocity, $U_{\mathrm{ms}}$ is given by

$$U_{\mathrm{ms}} = U_{\mathrm{mf}} + 0.07\sqrt{gD} \tag{12}$$

Bayens and Geldart (1974), however, reported that equation (12) is valid if $H_{\mathrm{mf}} > 1.3D^{0.175}$, otherwise, $U_{\mathrm{ms}}$ is expressed as

**Table VI.** Maximum likelihood of the correlation dimension obtained from the voidage fluctuation of the four 2D numerical simulations performed in this work

| Simulation | Det. 01 | Det. 02 | Det. 03 | Det. 04 | Det. 05 | Det. 06 |
|---|---|---|---|---|---|---|
| $P_3$ | 6.86 | 5.26 | 5.23 | 6.04 | 3.28 | 5.34 |
| $P_1$ | 5.22 | 4.43 | 4.42 | 5.04 | 2.53 | 4.79 |
| $P_1$-fine mesh simulation | 3.64 | 5.24 | 6.64 | 7.10 | 4.34 | 3.29 |
| $P_1$-low inlet gas velocity | 3.51 | 6.18 | 6.37 | 5.41 | 3.01 | 4.71 |

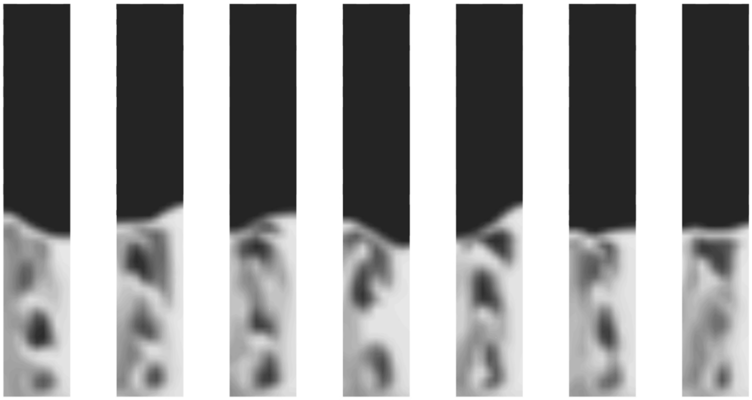

**(a)** $P_1$ simulation with low inlet gas velocity
**Note:** Diagrams drawn at every 0.50 seconds starting at 256.85 seconds

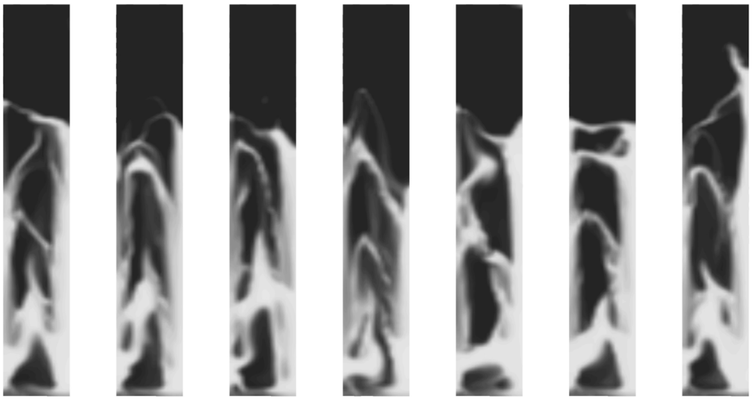

**(b)** $P_1$ simulation with a fine mesh
**Note:** Diagrams drawn at every 0.50 seconds starting at 162.55 seconds

**Figure 21.**
Simulation of a fluidized bed reactor operating (a) in the bubbling regime and (b) in the transition between bubbling and slugging regime

| Simulation | Det. 01 | Det. 02 | Det. 03 | Det. 04 | Det. 05 | Det. 06 |
|---|---|---|---|---|---|---|
| $P_3$ | 4.48 | 7.11 | 7.71 | 4.92 | 7.28 | 4.73 |
| $P_1$ | 3.68 | 4.82 | 4.95 | 4.19 | 4.60 | 3.83 |
| $P_1$-fine mesh simulation | 2.09 | 8.75 | 10.97 | 8.41 | 14.36 | 2.50 |
| $P_1$-low inlet gas velocity | 1.69 | 2.18 | 3.19 | 2.99 | 4.11 | 2.58 |

**Notes:** Maximum likelihood of the Kolmogorov entropy (in bits/s) obtained from the voidage fluctuation of the four 2D numerical simulations performed in this work

**Table VII.**

$$U_{\mathrm{ms}} = U_{\mathrm{mf}} + 0.07\sqrt{gD} + 0.16(1.3D^{0.175} - H_{\mathrm{mf}})^2 \tag{13}$$

where $H_{\mathrm{mf}}$ is the bed depth at minimum fluidization.

Most of the expressions available in the literature concerning slugging and transition regimes (see Smolders and Baeyens, 2001; Chen and Bi, 2003; Davidson *et al.*, 1985, for further details) were obtained by fitting well-controlled experimental data. Such experiments were mainly conducted with particles belonging to groups A and B of Geldart's powders classification and in narrow beds. In addition, wall effects and particles frictions were mostly neglected in the majority of these works (Smolders and Baeyens, 2001). In the bubbles shown in the last diagram of Figure 21(b), $\phi$ was $\approx 1.3$ and the minimum slugging velocity was $69.91\,\mathrm{cm\,s^{-1}}$. This intermittent slugging behavior result agree with the information obtained from maximum-likelihood estimation of the correlation dimension (Table VI).

However, the fluidization behavior described in equations (11)-(13) rely on both, the bed properties and the excess gas velocity, and do not take into account others effects such as bubble formation frequency. Cranfield and Geldart (1974) studied the fluidization of large particles ($1,000 \leq d_p \leq 200\,\mu$m) in relatively wide ($\approx 0.38\,\mathrm{m}^2$ of cross-section area) and deep ($\approx 0.35$ m) beds. They noticed that bubbles are formed some distance above the distributor and are initially circular without turbulent wakes. These bubbles rise and smoothly expand horizontally. They also reported that the bubble frequency at a given bed height is slightly dependent on the excess of gas velocity. The best fit of their data led to the following expression for the bubble frequency:

$$\mathscr{F} = 16.7H^{-0.72} \pm 20 \text{ percent} \tag{14}$$

where $H$ is the fluidized bed height. Noordergraaf *et al.* (1987), however, investigated the slug frequency of coarse particles fluidized in cylindrical beds 0.1 m wide and 1.0 m high. They found that the slug frequency, obtained from the PSD of pressure fluctuations may be expressed as

$$\mathscr{F} = 0.32\frac{U^{-0.15}}{H} \tag{15}$$

Table VIII shows the frequency obtained from equations (14) and (15) and from the PSD of pressure fluctuations in the simulations performed here. The obtained dominant frequencies do agree with the estimated frequencies calculated from the correlations and in particular with equation (15).

Bed expansions during the fluidization of coarse particles $489 \leq d_{\mathrm{p}}m \leq 3870\,\mu$m in slugging regime was studied by Baker and Geldart (1978). They investigated the

**Table VIII.** Slug frequencies calculated from equations (14) and (15) and obtained from the PSD of pressure fluctuations (detectors 2 and 3 – Table IV) of the simulations performed here

| Simulation | Detector | $\mathscr{F}^{\mathrm{corr}} \pm 20$ percent (Hz) (equation (14)) | $\mathscr{F}^{\mathrm{corr}}$ (Hz) (equation (15)) | $\mathscr{F}^{\mathrm{calc}}$ (Hz) |
|---|---|---|---|---|
| $P_3$ | 02 | 1.00 | 0.59 | 0.65 |
| | 03 | 0.61 | 0.29 | 0.33 |
| $P_1$ | 02 | 1.00 | 0.58 | 0.65 |
| | 03 | 0.61 | 0.29 | 0.28 |
| $P_1$-fine mesh simulation | 02 | 1.00 | 0.58 | 0.87 |
| | 03 | 0.61 | 0.29 | 0.45 |
| $P_1$-low inlet gas velocity | 02 | 1.00 | 0.65 | 0.77 |
| | 03 | 0.61 | 0.32 | 0.36 |

maximum bed height attained by slugging bed surface during a single oscillation ($H'_{max}$). Experiments carried out on systems with $2 \leq H_{mf}/D \leq 5$ resulted in a linear correlation between $H'_{max}$ and the excess of gas velocity

$$\frac{H'_{max}}{H_{mf}} = 1 + \frac{U'_{max} - U_{mf}}{0.35\sqrt{gD}} \tag{16}$$

where $U'_{max}$ is the maximum velocity reached during an oscillation. Instantaneous bed height calculated from equation (16) for a few snapshots are in good agreement with the observed bed height as shown in Table IX. In the range of gas velocities reached during the numerical simulations, $H_{max}$ may vary from 1.90 to 5.8 m for the simulation performed with a low inlet gas velocity and from 1.90 to 8.0 m for the other simulations.

Matsen *et al.* (1969) reported that the rise velocity of a slug, ($U_A$), in a freely slugging bed may be calculated through the following empirical correlation:

$$U_A = \sqrt{0.35gD} + U - U_{mf} \tag{17}$$

In the simulations performed here, no clear slug boundary could be observed, therefore, the slug rise velocity is estimated from a number of particle volume fraction distributions showing the rising of slugs and bubbles. Equation (17) suggests that the rise velocity of a slug may vary from 2.64 to 3.67 m s$^{-1}$, with the excess gas velocities shown in Table IX. The velocity of some of the slugs observed in the simulations oscillated from 0.75 to 3.50 m s$^{-1}$. Although this expression does take into account wall effects and excess gas velocities, it does neglect the influence of drag and the increasing of the bubble size due to coalescence.

In order to build-up a semi-empirical model that may predict the bubble sizes, Rowe (1976) fitted the few reported data from fluidization experiments. Such experiments involved particles of diameter up to 500 $\mu$m and superficial velocities of the order of magnitude of 0.40 m s$^{-1}$ and the following expression was suggested

$$d_B = (U - U_{mf})^{0.5}(H + \mathscr{H}_0)^{0.75}g^{0.25} \tag{18}$$

where $\mathscr{H}_0$ is a fitting parameter that may characterize the distributor. At the height of 0.56 m, i.e. half of the initial bed height, the mean bubble diameter calculated from equation (18) was 0.89 m. This means that the mean bubble diameter at this height is

**Table IX.** Several parameters calculated from semi-empirical correlations

| Simulation | t(s) | $H'_{max}$ (m) (equation (16)) | $H'_{max}$ (m) (simulation) | $U_A$ (m s$^{-1}$) (equation (17)) | $d_B$ (m) (equation (18)) |
|---|---|---|---|---|---|
| $P_3$ | 771.10 | 5.00 | 8.04 | 3.50 | 0.95 |
| $P_1$ | 394.55 | 5.55 | 5.91 | 3.56 | 0.97 |
| $P_1$-fine mesh simulation | 144.70 | 4.50 | 4.87 | 3.67 | 1.00 |
| $P_1$-low inlet gas velocity | 226.05 | 3.40 | 3.86 | 2.64 | 0.61 |

**Note:** (a) comparison between instantenous maximum bed height calculated from equation (16) and observed in the numerical simulations, (b) rise velocity of a slug (equation (17)) and (c) prediction of the mean bubble's size (equation (18)) at 0.80 m above the distributor nearly as wide as the bed diameter, however, in numerical simulations, it is very difficult to measure $d_B$ with accuracy. Therefore, by visual inspection of the animations produced from the simulations (see also Figures 7 and 21), it can be seen that the bubbles/slugs formed are approximately of the same diameter of the bed. Table IX shows the mean bubbles diameters calculated at 0.8 m above the distributor. In the transition between the fully bubbling and slugging regimes, as shown in the set of diagrams in Figure 8(a) (i.e. the simulation involving a lower inlet gas velocity), a relatively large bubble rises in the center region at a height of 0.8 m. The diameter of this bubble is 0.48 m while the calculated $d_B$ is 0.61 m. Reasons for such a discrepancy are possibly due to the experimental fitting parameter $\mathscr{H}_0$ and to the 2D geometry used here.

As the bubble formation is associated with the generation of power as described in the previous section, the correlations presented in this section are not necessarily accurate and must be used with caution.

*Surrogate model for time series prediction*

Prediction of chaotic phenomena is a major challenge due to the high computational cost associated with long-time numerical simulations. In addition, by predicting some processes parameters, such as gas pressure, temperature and voidage in fluidized beds, feedback controllers can be used to ensure safety and efficiency. Neural network methods (Platt, 1991; Moody and Darken, 1989) were successfully used to predict dynamical behavior in stationary and non-linear time series over a short time interval.

In this work, a kriging technique is used to interpolate the time series data generated by the $P_1$ and $P_3$ numerical simulations. A detailed description of kriging interpolation methods can be found in Stein (1999) and Olea (1999). In summary, kriging interpolation is a method which predicts unknown values from data observed at known locations. As the time series represents a surface in space-time, mapping of such a surface can lead to accurate interpolations in phase space and model predictions.

Let us first consider a finite time series $\Psi(x) = \{\Psi(x_1), \Psi(x_2), \ldots, \Psi(x_{n-1}), \Psi(x_n)\}$ spanning the $m$-dimensional phase-space. This time series is assumed to be stationary if the mean, variance and power spectra density are similar to the adjoining time series $\Psi(x+\delta) = \{\Psi(x_1+\delta), \Psi(x_2+\delta), \ldots, \Psi(x_{n-1}+\delta), \Psi(x_n+\delta)\}$ for any arbitrary distance, $\delta$. A set of $m$ non-sequential points of the points of the initial sequence are mapped into the surface $\mathscr{F} = \mathscr{F}\{\Psi(y), \Psi(y+\varepsilon), \ldots, \Psi(y+4\varepsilon)\}$ in phase space using kriging surface interpolation. The embedding dimension, $m$, of the fission power time series, calculated through the false nearest neighbors method (Hegger *et al.*, 1999; Kennel, 1997), represents the phase space that underlies the process and is equal to 5 for both the $P_1$ and $P_3$ simulations. A point in the 5D phase space then provides a predicted value for the fission power by interpolating the surface $\mathscr{F}$ using kriging. The prediction of the fission power $\Psi$ at time level $y+5\varepsilon$, $\Psi(y+5\varepsilon)$ is, therefore, obtained from the fission power at time levels $y, y+\varepsilon, \ldots, y+4\varepsilon$ and the surface $\mathscr{F}$, that is $\Psi(y+5\varepsilon) = \mathscr{F}\{\Psi(y), \Psi(y+\varepsilon), \ldots, \Psi(y+4\varepsilon)\}$ for some $\varepsilon = 0.2$. Then the time level $y$ is increased and the process repeated. If the time level $y$ is incrementally increased, an entire fission power time series can be generated.

This technique was applied to the fission rate and maximum temperature fluctuations of $P_3$ and $P_1$ simulations with a superficial gas inlet velocity of 120 cm/s and the predicted time series are shown in Figures 22(a), (b) and 23(a), (b). The predicted

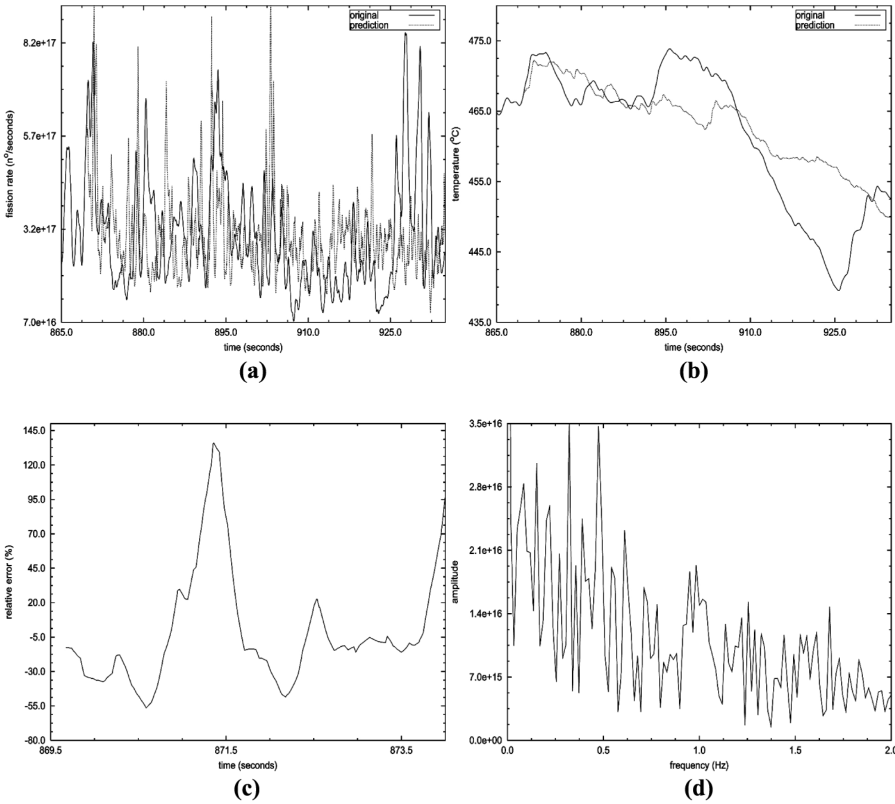


**Notes:** The average and variance of the fission rate in the whole original time series (after stationarity was reached) and in the predicted time series are $2.87 \times 10^{17}$, 1.30, $2.89 \times 10^{17}$ and 1.28, respectively

**Figure 22.**
$P_3$ simulation: original and prediction (a) fission rate and (b) maximum gas temperature fluctuation. The deviation of the (c) predicted fission rate from the original times series oscillates strongly, however, the dominant frequency (d) of the predicted segment is similar to the original time series (Figure 18(a))

fission rate fluctuation was compared with the original time series and although strong discrepancies were found, statistical properties, such as means, variance and power spectra densities were preserved.

In addition, the similarity between the PSD behavior (Figures 22(d) and 23(d)) of the predicted segment and the whole original time series, led to the investigation of a range of confidence in the prediction. A short-term prediction of fission-power may have a narrow range of confidence represented by:

$$\Psi(t) + \varepsilon(t) = \Psi_0 \exp(\sigma \Delta t) \tag{19}$$

where $\varepsilon$ is the error in the prediction, $\Psi_0$ is the initial fission-power and $\sigma$ is the exponential co-efficient. Hence, for an error up to 20 percent, the prediction technique can be applied to the $P_3$ and $P_1$ time series over approximately 2.50 and 1.50 s ($\sigma\{P_3\} = 0.3153$ and $\sigma\{P_1\} = 0.4808$), respectively. The gas temperature associated with the predicted fission rate is calculated through a simplified thermal balance equation:

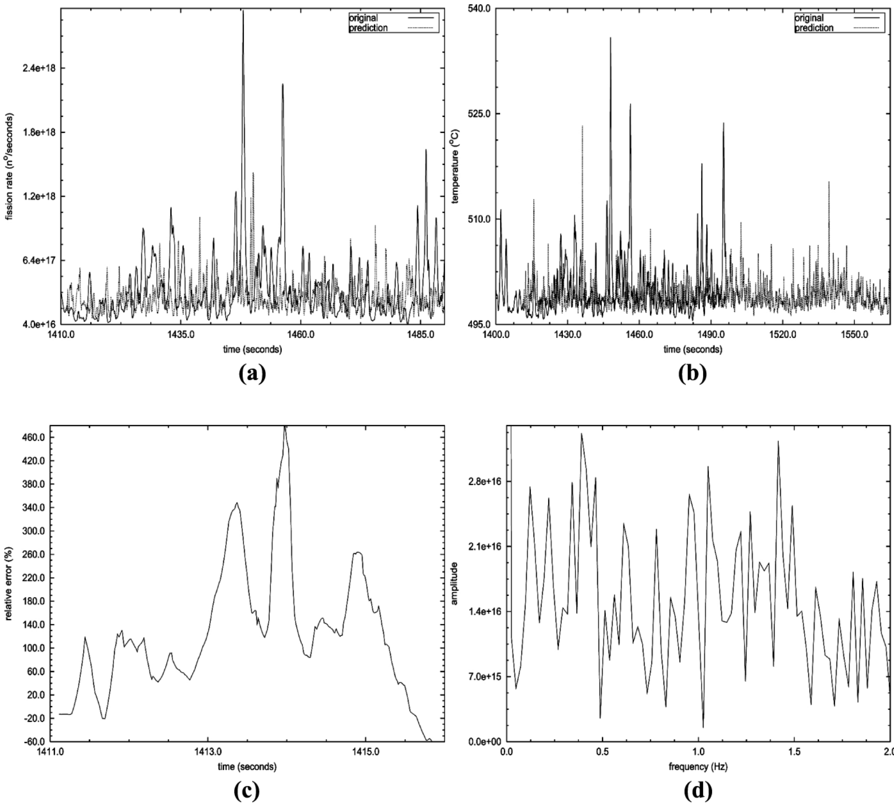


**Figure 23.**
$P_1$ simulation: original and prediction (a) fission rate and (b) maximum gas temperature fluctuation. The deviation of the (c) predicted fission rate from the original times series oscillates strongly, however, the dominant frequency (d) of the predicted segment is similar to the original time series (Figure 18(a))

**Notes:** The average (in $n^0$/seconds) and variance of the fission rate in the whole original time series (after stationarity was reached) and in the predicted time series are $2.73 \times 10^{17}$, 1.77, $2.76 \times 10^{17}$ and 1.74, respectively

$$\frac{\partial}{\partial t}[(C_\mathrm{s}M_\mathrm{s} + C_\mathrm{f}M_\mathrm{f})T_\mathrm{f}] + (\rho_\mathrm{f}C_\mathrm{f}v_\mathrm{f}\overline{A})\left(T_\mathrm{f} - T_\mathrm{f}^{(\mathrm{int})}\right) = \Psi \qquad (20)$$

$T_\mathrm{f}^{(\mathrm{int})}$ is the inlet gas temperature, $M_k$ and $\overline{A}$ are the mass of phase k and the bed cross section area, respectively. Given the fission-power, $\Psi$ (RHS of equation (20)) and an initial bed temperature, the bed temperature ($T_\mathrm{f}$) is calculated by solving equation (20) using a semi-analytical method. That is assuming $\Psi$ constant over a time interval and solving the resulting equations for the previous values of $T_\mathrm{f}$ with a new predicted temperature $T_\mathrm{f}$. This is repeated to construct the whole time series. A comparison between the predicted and original gas temperature fluctuations of $P_3$ and $P_1$ simulations over a short time interval are shown in Figures 22(b) and 23(b), respectively.

## Conclusions

This work investigates the numerical convergence and dynamics of a coupled neutron radiation and multiphase fluid flow system. That is a nuclear fluidized bed reactor particularly rich in dynamics and ideal for such an investigation. The dynamics associated with fission power fluctuations in the nuclear fluidized bed is investigated using deterministic chaos theory and autocorrelations.

The main conclusions from the applications are:

- The reactor can take over 5 min after start up to establish a quasi-steady-state and the mechanism for the long term oscillations of power have been established as a heat loss/generation mechanism.
- There is a clear need to parameterize the temperature of the reactor and, therefore, its power output for a given fissile mass or reactivity.
- The fission-power fluctuates by an order of magnitude with a frequency of 0.5-2 Hz. However, the thermal power output from gases is fairly steady.
- The fission-power oscillations depend on the neutron angle approximation. These preliminary results show smaller amplitude of power oscillations for neutron transport theory ($P_3$) then for diffusion theory ($P_1$). In addition the coordinate system ($r - z$ or $3 - D$) is shown to influence the dynamics.
- While the nuclear fluidized bed has reached a quasi-steady state after a few minutes of operation there are no signs of dynamic instability. Reactor start up seems particularly unpredictable in terms of the initial temperature rise, thus more work is required to investigate this as well as accident scenarios.
- There is a strong relationship between the bubbles production and the power released.
- The flow regime in chaotic fluidized bed can be statistically investigated through dynamical analysis. Such analysis can reveal interesting features related to the complexity of the flow.
- The variables solved in this problems, in particular the fission rate, can be predicted over a short time interval with a good range of confidence.

## Note

1. Animations concerning the following sections are available at: http://amcg.ese.imperial.ac.uk

## References

Anishchenko, V.S. (1995), *Dynamical Chaos – Models and Experiments: Appearance Routes and Strutucture of Chaos in Simple Dynamical Systems*, World Scientific, Singapore.

Bai, D., Bi, H.T. and Grace, J.R. (1997), "Chaotic behavior of fluidized beds based on pressure and voidage fluctuations", *AIChE Journal*, Vol. 43, pp. 1357-61.

Baker, C.G.J. and Geldart, D. (1978), "An investigation into the slugging characteristics of large particles", *Powder Technology*, Vol. 19, pp. 177-87.

Baskakov, A.P., Tuponogov, V.G. and Filippovsky, N.F. (1986), "A study of pressure fluctuations in a bubbling fluidized bed", *Powder Technology*, Vol. 45, pp. 113-17.

Basoglu, B., Brewer, R.W., Haught, C.F., Hollenbach, Wilkenson, A.D., Dodds, H.L. and Pasqua, P.F. (1994), "Simulation of hypothetical criticality accidents involving homogeneous damped low-enriched $UO_2$ powder systems", *Nuclear Technology*, Vol. 105, pp. 14-30.

Bayens, J. and Geldart, D. (1974), "An investigation into slugging fluidized beds", *Chemical Engineering Science*, Vol. 29, pp. 225-65.

Buyevich, Y.A., Yates, J.G., Chessman, D.J. and Wu, K-T. (1995), "A model for the distribution of voidage around bubbles in a fluidized bed", *Chemical Engineering Science*, Vol. 50, pp. 3155-62.

Casdagli, M.C. (1997), "Recurrence plots revisited", *Physica D*, Vol. 108, pp. 812-44.

Chen, A. and Bi, H.B. (2003), "Pressure fluctuations and transition from bubbling to turbulent fluidization", *Powder Technology*, Vol. 133, pp. 237-46.

Cranfield, R.R. and Geldart, D. (1974), "Large particle fluidisation", *Chemical Engineering Science*, Vol. 29, pp. 935-47.

Davidson, D.F., Clift, R. and Harrison, D. (1985), *Fluidization*, Academic Press, London.

de Oliveira, C.R.E., Pain, C.C. and Goddard, A.J.H. (1998), "The finite element method for time-dependent radiation transport applications", *Proceedings of the 1998 Radiation Protection and Shielding Topical Conference*, Nashville, USA, p. 343.

Ding, J. and Gidaspow, D. (1990), "A bubbling fluidization model using kinetic theory of granular flow", *AIChE Journal*, Vol. 36, pp. 523-38.

Duderstadt, J.J. and Hamilton, L.J. (1976), *Nuclear Reactor Analysis*, Wiley, New York, NY.

Gerwin, H. and Scherer, W. (1987), "Treatment of the upper cavity in a pebble-bed high temperature gas-cooled reactor by diffusion theory", *Nuclear Science and Engineering*, Vol. 97, pp. 9-19.

Gidaspow, D. (1994), *Multiphase Flow and Fluidization – Continuum and Kinetic Theory Descriptions*, Academic Press, Boston, MA.

Golovko, V.V., Kloosterman, J.L., van Dam, H. and van der Hagen, T.H.J.J. (1999), "Fuel particle design for a fluidized bed reactor", *Proceedings of Jahrestagung Kerntechnik '99, Annual meeting on nuclear technology '99*, Karlsruhe, Oldenburg, pp. 625-8.

Golovko, V.V., Kloosterman, J.L., van Dam, H. and van der Hagen, T.H.J.J. (2000a), "Investigation of a hypothetical start-up transient of a fluidized bed nuclear reactor", *Proceedings of Jahrestagung Kerntechnik 2000, Annual meeting on nuclear technology 2000*, pp. 581-4, Bonn.

Golovko, V.V., Kloosterman, J.L., van Dam, H. and van der Hagen, T.H.J.J. (2000b), "Analysis of transients in a fluidized bed nuclear reactor", *Proceedings ICENES 2000*, pp. 178-87, Petten.

Golovko, V.V., Kloosterman, J.L., van Dam, H. and van der Hagen, T.H.J.J. (2000c), "Dynamic core stability analysis of a fluidized bed nuclear reactor", *Proceedings of PHYSOR 2000*, pp. 63-75, Pittsburgh, PA.

Grassberger, P. and Procaccia, I. (1983a), "Characterization of strange attractors", *Physical Review Letters*, Vol. 50, pp. 346-9.

Grassberger, P. and Procaccia, I. (1983b), "Estimation of the kolmogorov entropy from a chaotic signal", *Physica Review A*, Vol. 28, pp. 2591-8.

Gulden, T.D. and Nickel, H. (1977), "Preface coated particle fuels", *Nuclear Technology*, Vol. 35, pp. 206-13.

Hegger, R., Kantz, H. and Schreiber, T. (1999), "Practical implementation of nonlinear time series methods: the TISEAN package", *Chaos*, Vol. 9, pp. 413-45.

Hetrick, D.L. (1993), *Dynamics of Nuclear Reactors*, American Nuclear Society, La Grange Park, IL.

Huilin, L., Gidaspow, D. and Bouillard, J.X. (1995), "Dimension measurements of hydrodynamic attractors in circulating fluidized beds", *AIChE Symposium Series*, Vol. 91, pp. 103-11.

Jenkins, J.T. and Savage, S.B. (1983), "A theory for the rapid flow of identical, smooth, nearly elastic spherical particles", *Journal of Fluid Mechanics*, Vol. 130, pp. 187-202.

Johnson, P.C. and Jackson, J. (1987), "Frictional-collisional constitutive relations for granular materials with application to plane shearing", *Journal of Fluid Mechanics*, Vol. 176, pp. 67-93.

Johnsson, F., Zijerveld, R.C., Schouten, J.C., van den Bleek, C.M. and Leckner, B. (2000), "Characterization of fluidization regimes by time-series analysis of pressure fluctuations", *International Journal of Multiphase Flow*, Vol. 26, pp. 663-715.

Kantz, H. and Schreiber, T. (2002), *Nonlinear Time Series Analysis*, Cambridge Univeristy Press, Cambridge, MA.

Kennel, M.B. (1997), "Statiscal test for dynamical nonstationary in observed time-series data", *Physical Review E*, Vol. 56, pp. 316-21.

Kimpland, R.H. and Korneich, D.E. (1996), "A two-dimensional multi-region computer model for predicting nuclear excursions in aqueous homogeneous assemblies", *Nuclear Science and Engineering*, Vol. 122, pp. 204-11.

Kunii, D. and Levenspiel, O. (1991), *Fluidization Engineering*, Butterworth-Heinemann, Boston, MA.

Leonard, B.P. (1991), "The ULTIMATE conservative difference scheme applied to unsteady one-dimensional advection", *Computing Methods in Applied Mechanics and Engineering*, Vol. 88, pp. 17-24.

Lun, C.K.K., Savage, S.B., Jeffrey, D.J. and Chepurniy, N. (1984), "Kinetic theories for granular flow: inelastic particles in Couette flow and slightly inelastic particles in a general flow field", *International Journal of Multiphase Flow*, Vol. 140, pp. 223-56.

Mather, D. and Barbry, F. (1991), "Examination of some fissile solution scenarios using CRITEX", *Proceedings of the Fourth International Conference on Nuclear Criticality Safety*, Oxford.

Mather, D., Buckley, A. and Prescott, A. (1994), "CRITEX – a code to calculate the fission release arising from transient criticality", AEA Report CS/R1007/R.

Matsen, J.M., Hovmand, S. and Davidson, J.F. (1969), "Expansion of fluidized beds in slug flow", *Chemical Engineering Science*, Vol. 24, pp. 1743-54.

Moody, J. and Darken, C.J. (1989), "Fast learning in networks of locally-tuned processing units", *Neural Computation*, Vol. 1, pp. 281-94.

Noordergraaf, I.W., Van Dijk, A. and Van den Bleek, C.M. (1987), "Fluidization and slugging in large particles systems", *Powder Technology*, Vol. 52, pp. 59-68.

Olea, R. (1999), *Geostatistics for Engineers and Earth Scientists*, Kluwer Academic Publishers, London.

Pain, C.C., Goddard, A.J.H. and de Oliveira, C.R.E. (1998a), "Finite element transient criticality code FETCH – verification and validation", *Proceedings of the Second NUCEF International Symposium on Nuclear Fuel Cycle*, Hitachinaka, Ibaraki.

Pain, C.C., de Oliveira, C.R.E. and Goddard, A.J.H. (1998b), "Modelling the criticality consequences of free surface motion in fissile liquids", *Proceedings of the Second NUCEF International Symposium on Nuclear Fuel Cycle*, Hitachinaka, Ibaraki.

Pain, C.C., de Oliveira, C.R.E., Goddard, A.J.H. and Umpleby, A.P. (2001a), "Transient criticality in fissile solutions – compressibility effects", *Nuclear Science and Engineering*, Vol. 138, pp. 78-95.

Pain, C.C., de Oliveira, C.R.E., Goddard, A.J.H. and Umpleby, A.P. (2001b), "Criticality behaviour of dilute plutonium solutions", *Nuclear Science and Technology*, Vol. 135, pp. 194-215.

Pain, C.C., de Oliveira, C.R.E. and Goddard, A.J.H. (2001c), "Non-linear space-dependent kinetics for criticality assessment of fissile solutions", *Progress in Nuclear Energy*, Vol. 39, pp. 53-114.

Pain, C.C., Mansoorzadeh, S. and de Oliveira, C.R.E. (2001d), "A study of bubbling and slugging fluidized beds using the two-fluid granular temperature model", *International Journal of Multiphase Flow*, Vol. 27, pp. 527-51.

Pain, C.C., Mansoorzadeh, S., de Oliveira, C.R.E. and Goddard, A.J.H. (2001e), "Numerical modelling of gas-solid fluidized beds using the two-fluid approach", *International Journal of Numerical Methods in Fluids*, Vol. 36, pp. 91-124.

Pain, C.C., Mansoorzadeh, S., Gomes, J.L.M.A. and de Oliveira, C.R.E. (2002a), "A numerical investigation of bubbling gas-solid fluidized bed dynamics in 2D geometries", *Powder Technology*, Vol. 128, pp. 56-77.

Pain, C.C., Gomes, J.L.M.A., Eaton, M.D., de Oliveira, C.R.E., Umpleby, A.P., Goddard, A.J.H., van Dam, H., van der Hagen, T.H.J.J. and Lathouwers, D. (2002b), "Space-dependent kinetics simulation of a gas-cooled fluidized bed reactor", *Nuclear Engineering and Design*, Vol. 219, pp. 225-45.

Pain, C.C., Eaton, M.D., Gomes, J.L.M.A., de Oliveira, C.R.E., Umpleby, A.P., Ziver, K., Ackroyd, R.T., Miles, B. and Goddard, A.J.H. (2003a), "An investigation of power stabilization and space-dependent dynamics of a nuclear fluidized-bed reactor", *Nuclear Science and Engineering*, Vol. 144, pp. 242-57.

Pain, C.C., Gomes, J.L.M.A., Eaton, M.D., de Oliveira, C.R.E. and Goddard, A.J.H. (2003b), "Numerical transport methods for radiation and multi-phase fluid flow modelling", *International Journal of Numerical Methods in Fluids*.

Platt, J. (1991), "A resource-allocating network for function interpolation", *Neural Computation*, Vol. 3, pp. 213-25.

Rifat, M., Al-Chalabi, R.M., Turinsky, P.J., Faure, F.X., Sarsour, H.N. and Engrand, P.R. (1993), "NESTLE: a nodal kinetics code", *Transactions of the American Nuclear Society*, Vol. 68, pp. 432-3.

Rozain, J. (1991), "Criticality excursions in wetted powder", *Proceedings of the Fourth International Conference on Nuclear Criticality Safety*, Oxford.

Rowe, P.N. (1976), "Prediction of bubble size in a gas fluidized bed", *Chemical Engineering Science*, Vol. 31, pp. 285-8.

Samuelsberg, A. and Hjertager, B.H. (1996), "An experimental and numerical study of flow patterns in a circulating fluidized bed reactor", *International Journal of Multiphase Flow*, Vol. 22, pp. 575-91.

Schouten, J.C. and van der Bleek, C.M. (1993), *RCHAOS, A Menu Driven Software Package for Chaotic Time Series Analysis*, Reactor research Foundation, Delft.

Schouten, J.C., Takens, F. and van der Bleek, C.M. (1994a), "Estimation of the dimension of a noisy attractor", *Physical Review E*, Vol. 50, pp. 1851-61.

Schouten, J.C., Takens, F. and van der Bleek, C.M. (1994b), "Maximum-likelihood estimation of the entropy of an attractor", *Physical Review E*, Vol. 49, pp. 126-9.

Schreiber, T. (1997), "Detecting and analysing nonstationarity in a time series using nonlinear predictions", *Physical Review Letters*, Vol. 78, pp. 843-6.

Sefidvash, F. (1996), "Status of the small modular fluidized bed light water nuclear reactor", *Nuclear Engineering Design*, Vol. 167, pp. 203-14.

Smolders, K. and Baeyens, J. (2001), "Gas fluidized beds operating at high velocities: a critical review of occurring regimes", *Powder Technology*, Vol. 119, pp. 269-91.

Stein, M.L. (1999), *Interpolation of Spatial Data: Some Theory for Kriging*, Verlag-Stein, Berlin.

Stewart, P.S.B. and Davidson, J.F. (1967), "Slug flow in fluidised beds", *Powder Technology*, Vol. 1, pp. 61-80.

van Dam, H., van der Hagen, T.H.J.J., Hoogenboom, J.E., Khotylev, V.A. and Mudde, R.F. (1997), "Statics and dynamics of a fluidized bed fission reactor", *Proceedings of the International Conference of Emerging Nuclear Energy Systems*, pp. 609-16, Tel-Aviv, Israel.

van der Stappen, M.L.M., Schouten, J.C. and van der Bleek, C.M. (1993), "Application of deterministic chaos theory in understanding the fluid dynamic behavior of gas-solids fluidization", *AIChE Symposium Series*, Vol. 89, pp. 91-102.

WIMS8A: User Guide for Version 8 (1999), *AEA Technology Report ANSWERS/WIMS*, Vol. 9.

Yaffee, R.A. and McGee, M. (2000), *Introduction to Time Series Analysis and Forecasting with Applications of SAS and SPSS*, Academic Press, New York, NY.

Yamamoto, Y. (1995), "Space-dependent kinetics analysis of a hypothetical array criticality accident involving units of aqueous uranyl fluoride", *Proceedings of the Fifth International Conference on Nuclear Criticality Safety*, pp. 10-19, Albuquerque, New Mexico.

Yu, D., Lu, W. and Harrison, R.G. (1998), "Space time index plots for probing dynamical nonstationarity", *Physical Letters A*, Vol. 250, pp. 323-7.

## Further reading

Mori, S. and Wen, C.Y. (1975), "Estimation of bubble diameter in gaseous fluidized beds", *AIChE Journal*, Vol. 21, pp. 109-15.

Schreiber, T. and Schmitz, A. (2000), "Surrogate time series", *Physica D*, Vol. 142, pp. 346-82.

Smith, L.A. (1992), "Identification and prediction of low dimensional dynamics", *Physica D*, Vol. 58, pp. 50-76.

Theiler, J., Eubank, S., Longtin, A., Galdrikian, B. and Farmer, J.D. (1992), "Testing for nonlinearity in time series: the method of surrogate data", *Physica D*, Vol. 58, pp. 77-94.